THE DAMPING OF SURFACE WATER WAVES IN CONTAINERS WITH GROOVED SURFACES

by

LORNE EDWARD GETTEL
B.Sc., The University of British Columbia, 1974

A THESIS SUBMITTED IN PARTIAL FULFILMENT OF
THE REQUIREMENTS FOR THE DEGREE OF
MASTER OF SCIENCE

in the Department
of
PHYSICS

We accept this thesis as conforming to the
required standard

THE UNIVERSITY OF BRITISH COLUMBIA

September 1975

In presenting this thesis in partial fulfilment of the requirements for an advanced degree at the University of British Columbia, I agree that the Library shall make it freely available for reference and study. I further agree that permission for extensive copying of this thesis for scholarly purposes may be granted by the Head of my Department or by his representatives. It is understood that copying or publication of this thesis for financial gain shall not be allowed without my written permission.

Department of Physics

The University of British Columbia
2075 Wesbrook Place
Vancouver, Canada
V6T 1W5

Date October 6, 1975

ABSTRACT

The damping of surface waves on shallow water can be affected by the roughness of the container walls as well as by surfactant layers present on the air-water interface. The increase in the damping caused by a grooved wave tank base has been studied both theoretically and experimentally. In any experimental investigation into the effect of surface roughness on the damping, surfactants can obscure the effects of wall roughness. An experimental technique is described to enable the relative importance of these two effects to be determined unambiguously. Initially experiments were conducted with the groove amplitude much smaller than the viscous boundary layer thickness. It was found that the increase in the damping caused by the grooved base was small (< 5% increase).

The damping has also been studied for large amplitude grooves on the base of the wave tank (dimensions much larger than the viscous boundary layer thickness). It is shown theoretically that, for grooves of triangular or approximately sinusoidal cross section, the damping is increased by an

amount proportional to the total surface area of the grooved surface, and is independent of the direction of flow with respect to the grooves. The theoretical model applies when the groove spacing and amplitude are small compared to the fluid depth and wavelength of the surface waves, but are large compared to the viscous boundary layer thickness. Experiments were conducted to test these predictions. By carrying out observations on two surface modes, it is shown that the observed increased damping is due to the grooved surface alone and cannot be attributed to spurious surfactant effects. It was found experimentally that the damping was independent of flow direction with respect to the grooves, and the increase in the damping was strictly proportional to the fractional increase in the area of the base, in complete agreement with the theoretical predictions.

TABLE OF CONTENTS

		Page
ABSTRACT		ii
LIST OF TABLES		vi
LIST OF FIGURES		vii
ACKNOWLEDGMENTS		x
NOMENCLATURE		xi
Chapter		
1	INTRODUCTION	1
	PART A	
2	THE EFFECT OF SMALL AMPLITUDE WALL ROUGHNESS ON THE DAMPING OF SURFACE WAVES	4
	2.1 Introduction	4
	2.2 Calculation of the Damping Frequency for a Grooved Base	8
3	DAMPING EXPERIMENTS FOR SMALL ROUGHNESS AMPLITUDE	13
	3.1 Experimental Set-up	13
	3.2 Experimental Results	22

Chapter Page

3.3 Discussion 36

3.4 Conclusions. 40

PART B

4 THE EFFECT OF LARGE GROOVES ON THE DAMPING OF SURFACE WAVES 42

4.1 Introduction 42

4.2 Theory 45

4.3 Calculation of $\int SdA$ for Grooved Surfaces 50

4.4 Calculation of the Damping Frequency. 62

5 DAMPING EXPERIMENTS FOR LARGE AMPLITUDE GROOVES. 68

5.1 Experimental System. 68

5.2 Experimental Results and Discussion 77

5.3 Conclusions. 86

REFERENCES 87

APPENDICES

A THE GENERAL RESULT FOR THE DAMPING FREQUENCY 89

LIST OF TABLES

Table		Page
1	The Experimental Conditions for the Circular Wave Tank Experiments.	10
2	The Experimental Conditions for the Square Wave Tank Experiments.	71
3	Values of the Damping Frequency	85

LIST OF FIGURES

Figure		Page
1	Orientation of driver electrode with respect to the grooved base of the wave tank.	7
2	Cross-section of the circular wavetank	14
3	Mounting system for the driver electrode	16
4	Plan view of the optical detection system.	19
5	Photoresistor detection circuit.	20
6	Damping runs for a smooth aluminum base.	24
7	Damping runs for a grooved aluminum base (two smooth quadrants)	25
8	Damping runs for 33 r.p.m. record used as a base (two smooth quadrants).	26
9	Damping runs for a grooved aluminum base ("dirty surface").	27
10	The logarithm of wave amplitude vs time for a smooth base.	28
11	The logarithm of wave amplitude vs time for a grooved aluminum base.	29

Figure		Page
12	The logarithm of wave amplitude vs time for a 33 r.p.m. record used as a base.	30
13	The logarithm of wave amplitude vs time for a grooved aluminum base (contaminated surface)	31
14	Damping frequency vs θ (smooth base)	32
15	Damping frequency vs θ (grooved aluminum base) . .	33
16	Damping frequency vs θ (33 r.p.m. record used as a base)	34
17	Damping frequency vs θ (grooved aluminum base, contaminated surface).	35
18	Mapping of a polygonal region into the upper half of the w plane.	53
19	Features of groove geometry.	55
20	Coordinate system used for the calculation of the damping frequency	63
21	Cross-section of the square wave tank.	69
22	High voltage waveform generation circuit	73
23	Function generator	74
24	The construction of an arbitrary waveform using the function generator	76
25	Damping runs for $\lambda = 2/3$ L	79
26	Damping runs for $\lambda = 2$L.	80

Figure | Page

27 The logarithm of wave amplitude vs time (λ = 2/3 L) 81

28 The logarithm of wave amplitude vs time (λ = 2L) 82

ACKNOWLEDGMENTS

I sincerely wish to express my thanks to Dr. F.L. Curzon for his excellent supervision during the course of this work.

I would like to thank Ralph Pudritz for his help in calculating the inviscid flow potential over grooved boundaries. The assistance of Jim Aazam-Zanganeh in the design of the counting logic, and Peter Chen who helped with the early experiments, is gratefully acknowledged. I would also like to thank Sharon Haller for an excellent typing job.

Financial assistance from the National Research Council has been gratefully received.

This work was supported by a grant from the Atomic Energy Control Board of Canada.

NOMENCLATURE

a	groove amplitude
f	frequency of surface modes
i	$\sqrt{-1}$
k	surface mode wavenumber
ℓ	viscous boundary layer thickness
$\underline{n}$	unit vector normal to a surface of the wave tank
v	flow velocity
v_0	inviscid flow velocity
w	complex variable
x,y,z	position coordinates
A	amplitude of surface waves
A'	area ratio
B	Beta function
H	fluid depth
J	Bessel Function

L	length of the square wave tank
P	fluid pressure
R	radius of circular wave tank
S	viscous energy dissipation per unit area
η	coordinate along $\underline{n}$
θ	angle between the nodal line of the surface wave and the edge of one of the groove quadrants on the base of the wave tank
λ	wavelength of surface mode
ν	kinematic viscosity
ξ	wavelength of groove spacing
ρ	fluid density
σ	damping frequency
ϕ	inviscid flow velocity potential
ω	angular frequency of surface mode

Chapter 1

INTRODUCTION

The damping of surface waves on a fluid can be affected by surfactants on the free surface of the fluid, or by the roughness of the container walls. In the past, wall roughness has been used, with little justification, as a convenient means of explaining discrepancies between theory and experiment for the damping of surface waves [Case and Parkinson, 1957].

In this investigation the effect of wall roughness on the damping of standing surface waves has been examined. The surface waves used in this work were excited by spatially inhomogeneous, time periodic electric fields applied normally to the free fluid surface. In all of this work the wave amplitude of the surface wave was sufficiently small so that linear theory could be used. That is, the wave amplitude was much smaller than the wavelength of the surface mode. The dimensions of the wall roughness can be divided into two regimes: larger or smaller than the viscous boundary layer thickness. In Part A, the case where the roughness

amplitude is smaller than the viscous boundary layer thickness is examined. In this investigation a cylindrical wave tank is used. The roughness structure is controlled by inserting grooved plates on the base of the wave tank.

We realized through the course of these experiments that groove amplitudes much smaller than the viscous boundary layer thickness had little effect on the damping, contrary to previous conjecture [Case and Parkinson, 1957]. This prompted us to examine the affect on the damping caused by large grooves ($a >> \ell$), where a is the roughness amplitude, and ℓ is the viscous boundary layer thickness. In part B, we examine this case both theoretically and experimentally. For these experiments a square wave tank is used to simplify the analysis. The groove structure was controlled in the same manner as in our initial experiment; a grooved plate was inserted on the bottom of the wave tank.

Part A is composed of Chapter 2 and 3. Chapter 2 consists of an introduction to the effects of surface roughness and surfactant layers on the damping. In addition the damping frequency is calculated for a wave tank base with two grooved quadrants. Chapter 3 describes the experimental setup and results for small groove size ($a < \ell$).

Part B consists of Chapter 4 and 5. Chapter 4 consists of a general approach applicable for determining the damping enhancement caused by grooved container walls. Using this

approach the damping frequency is determined for some given groove structures. Chapter 5 describes the experimental system used to check the predictions of Chapter 4, and the experimental results are compared with these predictions. In addition, Chapter 5 also consists of a discussion of the major conclusions of these investigations and suggestions for future work.

PART A

Chapter 2

THE EFFECT OF SMALL AMPLITUDE WALL ROUGHNESS ON THE DAMPING OF SURFACE WAVES

2.1 Introduction

Wall roughness has been used in the past [Case and Parkinson, 1957] to explain discrepancies between theory and experiment for the damping of surface waves. Case and Parkinson studied the damping of water waves in cylindrical vessels of circular cross section and found that, for shallow water the damping was a factor of three larger than their theoretical value. They attributed this discrepancy to the surface roughness of their cylindrical vessels, even though the amplitude (depth) a of the roughness structure of their vessels was small compared to the viscous boundary layer thickness, ℓ. It is difficult, however, to envisage a physical mechanism which could produce a significant increase in the damping, if $a \ll \ell$. Essentially for laminar flow, the fluid in contact with the container walls is at rest in a layer of thickness $\sim \ell$. For $a \ll \ell$ no information about the roughness structure should be propagated into the fluid. As stated previously, surfactant layers present on the air-water interface can significantly increase the

damping of surface waves [see Levich, 1941, 1962; Dorrestein, 1951; and Pike and Curzon, 1968].

Surfactant layers on the free fluid surface alter the lateral mobility of this surface. On shallow fluids the damping essentially doubles as the surface becomes laterally immobilized (i.e. the air-water interface is completely covered by a surface film) [see Pike and Curzon, 1968].

The surface film can essentially be viewed as a thin elastic membrane, which is stretched or compressed by the motion of the fluid. This results in the appearance of additional forces at the surface which must be taken into account in the boundary conditions at the free surface. Surfactant layers on the top of the fluid can arise from surfactant residues left on the vessel walls which travel upwards to the free surface, and to residues deposited on the surface from the air above it. For the former, the effect is more serious for shallow fluids, since the free water surface is closer to the container base, decreasing the time required for surfactants to reach the air water interface. Hence, the enhancement in the damping reported by Case and Parkinson could be due to surfactant layers present on the air-water interface or to surface roughness.

In this investigation, we set out to determine experimentally the effect on the damping of surface waves

due to container roughness satisfying $a < \ell$. This task is greatly complicated by the presence of surfactants, which can obscure roughness effects. Thus, it is essential to design our experiments so that these two effects can be separated. In the experimental investigation used to separate these effects, the damping was studied for a sloshing mode excited on shallow water in a vessel with alternately roughened quadrants on the base (see Figure 1). If the roughened surfaces of the container do cause enhanced damping, then the damping frequency will vary sinusoidally with θ, where θ is the angle between the nodal line of the surface wave and the edge of one of the grooved quadrants on the base of the vessel (see Figure 1). During the time required for a series of measurements the condition of the air-water interface can change due to surfactants, which will alter σ. These variations in σ, however, will not have any angular dependence, and if the time required to measure σ is small, then these variations in σ due to changes in surfactant concentration should be small. In fact, it was found that σ for a given value of θ changes by less than $\pm$ 5% during the time required to perform an angular scan of σ. Hence if roughened surfaces do increase σ by a factor of three [Case and Parkinson], then it should be possible to observe a sinusoidal dependence of σ on θ which is not obscured by surfactant effects.

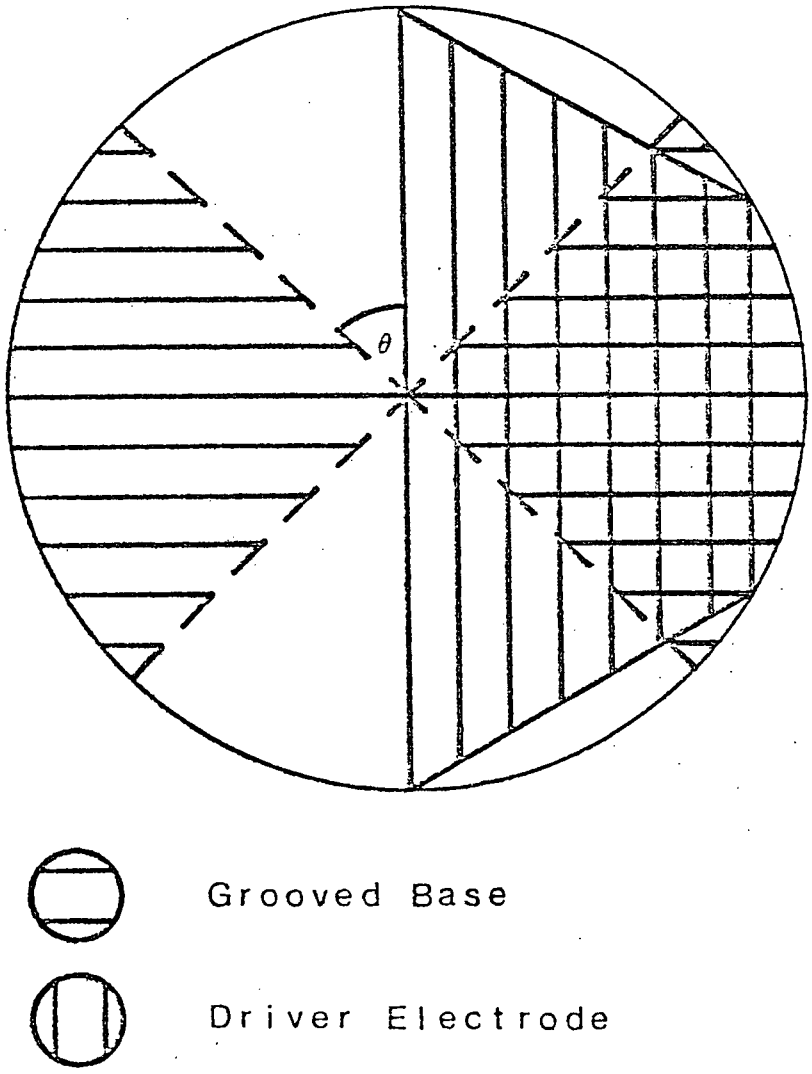

Figure 1. Orientation of driver electrode with respect to the grooved base of the wave tank.

In the next section the damping frequency is calculated for the grooved quadrant bases used in the experimental study.

2.2 Calculation of the Damping Frequency for a Grooved Base

The damping frequency will now be calculated for a sloshing mode for a shallow fluid in a wave tank with a pair of grooved quadrants on the base. The nodal line of the surface wave is inclined at an angle θ to the edge of one of the grooved quadrants. Case and Parkinson show that the damping frequency can be written as

$$\sigma = \sigma_W + \sigma_B + \sigma_{MS} \tag{2.1}$$

where σ_W, σ_B, and σ_{MS} are the contributions made, respectively by the walls of the wave tank, the base, and at the fluid surface, which is assumed to be laterally mobile. In all of our experiments, however, the fluid surface was laterally immobile. The term σ_{MS} must then be replaced by σ_{IS}, the laterally immobile term, where

$$\sigma_{IS} = \sigma_B \, \mathrm{Cosh}^2 \, (kH) \tag{2.2}$$

k = wave number of the surface mode

H = fluid depth

[see Pike and Curzon, 1968].

For the conditions used in the experiments $kH \ll 1$ (see Table 1), and $\sigma_{IS} \simeq \sigma_B$ for a smooth base. The fluid is shallow so that $\sigma_W/\sigma_{IS} \ll 1$ and the σ_W term can be neglected. The damping frequency for a smooth base is then given by

$$\sigma_1 = 2\,\sigma_{IS} \tag{2.3}$$

The damping frequency is in general dependent upon the inviscid flow velocity on the container walls (see Section 4.2) and Appendix A)

$$\sigma \propto \int v_0^2\, dA \tag{2.4}$$

where v_0 is the inviscid flow velocity tangential to a surface of the container, and dA is an area element on the surface. For a roughened surface (2.4) is increased according to Case and Parkinson. It will be assumed that the roughness structure for $a < \ell$ does not alter the inviscid flow velocity v . The damping frequency for a roughened surface could then be given by

$$\sigma \propto \int A'\, v_0^2\, dA \tag{2.5}$$

where A' is a constant, $A' > 1$.

Table 1

Experimental Conditions

Features of the water tank	
Depth, H	= (4.33 ± 0.01) cm
Radius, R	= (15.0 ± 0.1) cm
Kinematic viscosity	= 0.01 $cm^2 sec^{-1}$
Characteristics of 'sloshing-mode'	
Dimensionless wave number, kR	= 1.8412
Oscillation frequency, f	= (1.221 ± 0.001) Hz
Damping frequency σ_0 (smooth base)	= (0.043 ± .006) Hz
Boundary layer thickness = $\sqrt{\nu/\omega}$	= 0.36 mm
Properties of Grooved Quadrants	
a) 33 r.p.m. record - groove spacing	= 0.063 mm
b) Aluminium discs - groove spacing	= 1 mm or 3.1 mm (i.e. 1/8")

The damping frequency, σ_2 for the roughened quadrants on the base will now be calculated using the approach used for (2.5),

$$\sigma_2/\sigma_{IS} = \frac{1 + \int_{\theta}^{\theta+\pi/2} (A' v_0^2)\, r\, dr\, d\phi + \int_{\theta+\pi/2}^{\theta+\pi} v_0^2\, r\, dr\, d\phi}{\int_{\theta}^{\theta+\pi} v_o^2\, r\, dr\, d\phi} \qquad (2.6)$$

where (r,ϕ) are polar co-ordinates on the base of the wave tank and v_0 is the tangential velocity for a sloshing mode for an inviscid fluid. For a sloshing mode

$$v_0 = \text{constant } J_1(kr) \cos \phi \qquad (2.7)$$

where $\frac{\partial}{\partial r} J_1(kr) = 0$ at $r = R$, the outer edge of the wave tank [see Case and Parkinson]. Now eliminating v_0 from equation (2.6) and using equation (2.3) to eliminate σ_{IS} yields

$$\frac{\sigma_2}{\sigma_1} = 1/2 + 1/4(1 + A') - 1/2\, \pi(A' - 1) \text{ Sin } 2\theta \qquad (2.8)$$

Thus the damping frequency should vary sinusoidally with θ for the base considered, if roughness satisfying $a < \ell$ does enhance the damping.

The expressions for σ_B and σ_W for a cylindrical wave tank were derived by Case and Parkinson. They are

$$\sigma_B = \left(\frac{\omega_{SU}\ \nu}{2}\right)^{\frac{1}{2}} k \operatorname{cosech}(2kH) \tag{2.9}$$

$$\sigma_W = \left(\frac{\omega_{SU}\ \nu}{2}\right)^{\frac{1}{2}} \frac{1}{2R}\left[\frac{1 + (s/kR)^2}{1 - (s/kR)^2} - \frac{2kH}{\sinh(2kH)}\right] \tag{2.10}$$

where R is the radius of the wave tank, k is the wave number of the surface mode, H is the fluid depth, and ω_{SU} is the frequency characterizing the surface mode. The ω_{SU}'s are given by

$$\omega_{SU}^2 = g\, k_{SU} \tanh(k_{SU} H) \tag{2.11}$$

for surface gravity waves.* The k_{SU} satisfy

$$J_S'(k_{SU} R) = 0 \tag{2.12}$$

For the sloshing mode S = U = 1. The explicit forms for σ_W and σ_B are mentioned since a comparison between predicted σ (laterally mobile or immobile) and experimental σ determines the condition of the top surface of the fluid.

*Note that equation (2.11) is the general dispersion relation for gravity waves. For an unbounded system there is of course no restrictions on the values of the wave number.

Chapter 3

DAMPING EXPERIMENTS FOR SMALL ROUGHNESS AMPLITUDE

3.1 Experimental Set-up

When studying the damping of surface waves either temporal or spatial damping can be considered. Temporal damping involves the use of standing waves, while travelling waves are used for spatial damping. Throughout our experimental investigations temporal damping has been considered. There are three major advantages to this approach. When a standing wave system is considered, it is possible to drive the system resonantly to obtain a pure surface mode, with an amplitude that can easily be detected. The wave amplitude detector for such a system can be at a fixed position and only one detector is required. Spatial damping requires wave tank dimensions of at least the order of the damping length, which is much larger than the wavelength of the surface mode. This necessitates large systems, which is not the case for temporal damping.

The geometry of the wave tank is shown in Figure 2. The tank is made from a section of an old glass bell jar with

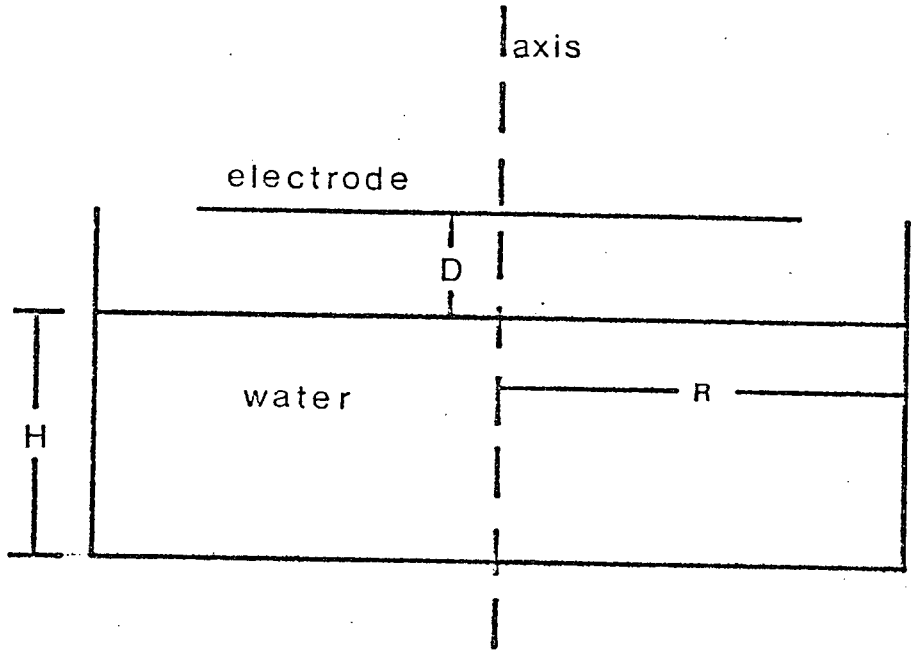

Figure 2. Cross-section of the circular wave tank.

the ends ground parallel to each other. The lower end of the tank is sealed to a copper sheet by a silicone adhesive on the outside surface of the tank. The copper sheet is mounted on a conventional levelling table fitted with three adjustable legs. The depth of water in the tank can be measured at any location by a micrometer depth gauge. This device, together with the three adjustable legs, enables the free surface of the fluid to be aligned parallel to the base of the wave tank to an accuracy of approximately 0.04 cm.

The waves are excited by a horizontal electrode mounted above the fluid surface (Figure 2). The electrode is made from a hexagonal piece of printed circuit board with a 1.4 cm wide strip of copper removed from one diameter. A vertical vane is mounted below the electrode along a diameter at right angles to the insulating strip. The vane suppresses spurious sloshing modes which caused some problems in our early experiments (see Discussion).

The electrode just fits inside the wave tank and is suspended from a lucite frame which is fixed across the top of the tank. The suspension system consists of three spring loaded micrometers mounted at the vertices of an equilateral triangle (Figure 3). After the tank is level, three identical gauge pins are placed on the bottom and the micrometers are adjusted until the electrode just rests on the pins. The frame and electrode are then removed so that

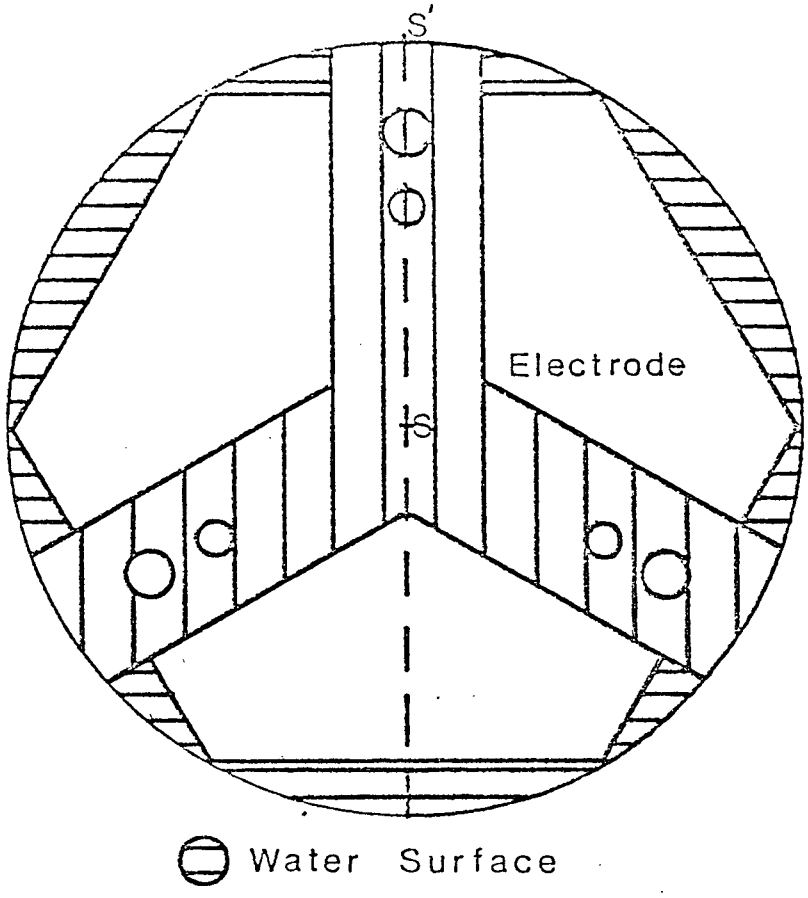

a

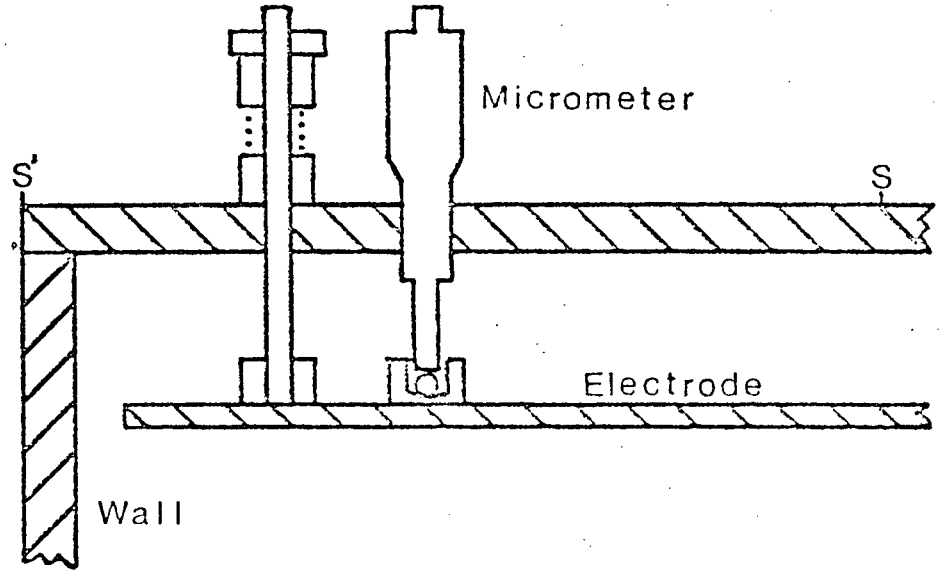

b

Figure 3. Mounting system for the driver electrode.
(a) Plan view of micrometer support frame.
(b) The micrometer levelling system.

the metal gauge pins can be taken out of the tank. When the electrode and holder are replaced, checks with a travelling microscope show that the electrode and water surface are spaced by a constant distance of ~ 1 cm ± 0.1 mm.

The electrode plate can be rotated about a vertical axis, and angular position can be measured to an accuracy of ± 1° with a protractor scale fixed around the upper edge of the wave tank. By applying a time dependent high voltage to one-half of the electrode sloshing modes can be excited on the water surface. The nodal line of the wave is along the insulated diameter of the electrode, which can be set at any compass direction by rotating the plate about its vertical axis. The frequency of the high voltage waveform is adjusted to resonate with the sloshing mode (~ 1.22 Hz in our experiment). This result is approximately determined from equation (2.11), where k satisfies equation (2.12). The sloshing mode considered is the fundamental and for this kR = 1.84. The dispersion relation given by (2.11) is not completely correct when an electric field is applied normally to the surface; there is a small additional term in the dispersion relation proportional to $-E^2$ (where E = electric field) (see Ionides thesis). This shifts the resonant frequency by a small amount. Once the E field is shut off, however, the surface modes oscillate at the natural frequency given by equation (2.11). The form of the high voltage

waveform used is given by $V = V_0(1 + \cos\omega t)^{\frac{1}{2}}$. The H.V. waveform generator essentially consists of a rotary switch with appropriate resistor networks to produce the waveform given above. Complete details of this generator are given in [Ionides Thesis, 1972] and [Phillips and Curzon, 1973] and will not be stated here.

The maximum voltage used is 5KV, which produces a wave amplitude of ~ 2 mm on the water surface. The wave amplitude is observed with a microscope (magnification x35) focused on the air water interface at a distance of ~ 2 cm in from the wall of the wave tank. The microscope can be displaced horizontally to ensure that it is never focused on the water surface along a nodal line. The eyepiece of the microscope is fitted with a photoresistor. Another photoresistor monitors a constant light source behind the wave tank used to illuminate the tank (see Figure 4). After processing of these two signals (see Figure 5), they are applied to a differential amplifier (Tektronix storage oscilloscope (549) equipped with a 1A2 differential amplifier). This procedure eliminates noise signals common to both inputs. For complete details of this measuring system see [Ionides, 1972; Curzon and Phillips, 1973].

The grooved surface on the base of the wave tank is produced by inserting suitably grooved discs and taping them down to the base of the tank with vinyl tape. This

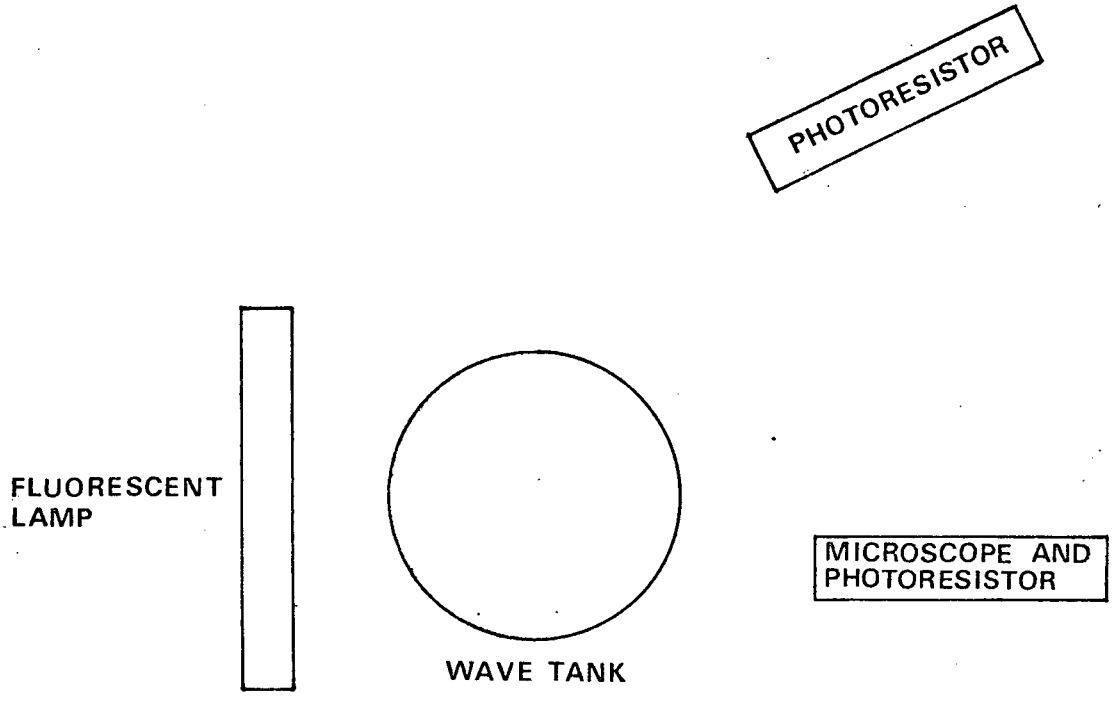

Figure 4. Plan view of the optical detection system.

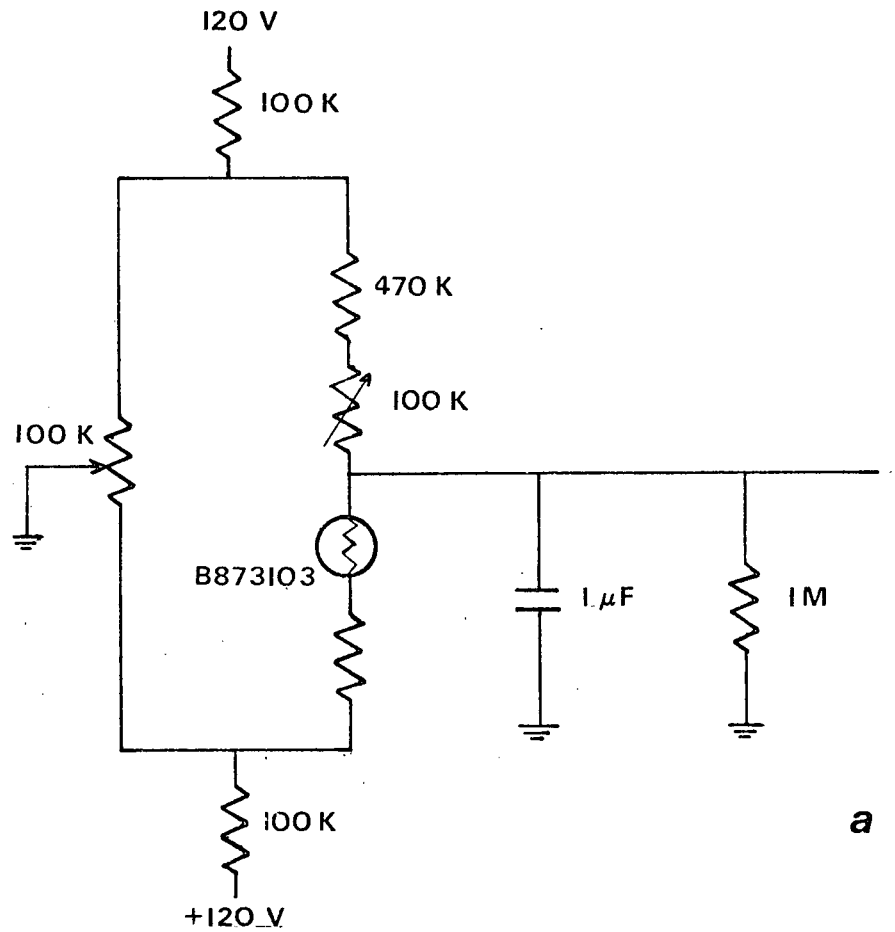

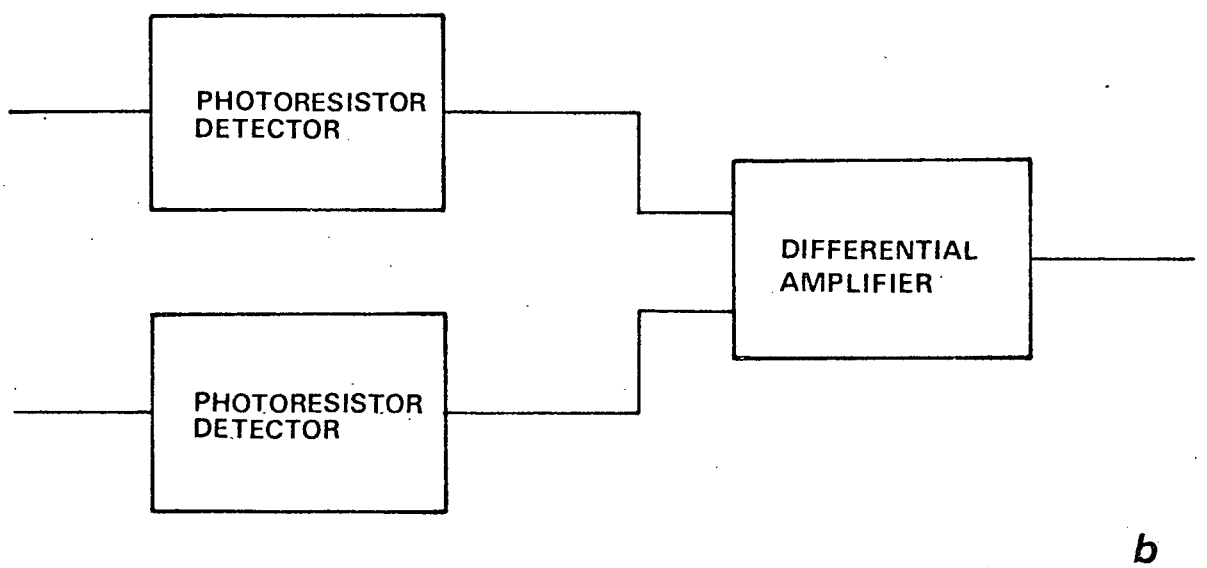

Figure 5. Photoresistor detection circuit. (a) Circuit of one of the photoresistor detectors. (b) Differential photoresistor network.

procedure is necessary in order to prevent anomalous wave damping caused by seepage of water under the grooved disc (see Discussion).

A number of different grooved discs were used in these experiments. In all cases the groove amplitude was smaller or at least ~ boundary layer thickness ℓ. For small groove widths and amplitudes we used phonograph records (33 r.p.m.). The grooves of a pair of opposite quadrants were eliminated by varnishing these regions. For groove widths larger than ~ 0.5 mm we cut concentric grooves on an aluminum plate (~ 5 mm thick), using a lathe. Grooves in two opposite quadrants were removed, using a milling machine.

To perform the experiment, surface waves were excited with the wave generation electrode. Once the wave amplitude has stabilized, the generator was switched off, and the decay of wave amplitude was observed on the storage oscilloscope. By judiciously changing the gain of the oscilloscope amplifier during the course of the decay, the signal could be kept large enough to ensure accurate measurement. The damping freuqency was determined from the slope of the logarithmic plot of the wave amplitude as a function of time.

3.2 Experimental Results

Experiments were initially conducted to determine the damping frequency for a sloshing mode with a smooth base. This was done to determine the condition of the top surface of the fluid. It was found experimentally that $\sigma_0 = 0.043 \pm 0.006$ sec^{-1}, where σ_0 is the damping frequency for a smooth base. There was quite a large variation in σ from run to run, depending on the condition of the distilled water. This result compared favourably with the predicted laterally immobile result for σ. Using equations (2.2), (2.9), and (2.10), this predicted result was $\sigma = 0.0456$, for the experimental conditions given in Table 1. Thus the fluid surface used in our experiments was laterally immobile.

Experiments were then conducted to determine the damping frequency for a sloshing mode with a grooved disc, as described in Section (3.1), secured on the bottom of the wave tank. With such a base, according to our calculation in Section (2.2), the damping frequency should vary sinusoidally with θ, where θ is the angle between the nodal line of the sloshing mode and an edge of the grooved quadrant (see Figure 1).

In our early experiments we observed that σ varied with θ (large variations up to $\sim 2\ \sigma_0$), and thus we thought we had established an effect attributable to surface roughness. This turned out, however, not to be the case. The variation

in σ with θ was in fact caused by either water getting under the grooved base or the excitation and interaction of spurious modes. The seepage of water under certain parts of the disc would result in enhanced damping when the flow velocity was at a maximum over these regions. When the flow direction was varied, the enhancement would also vary, resulting in an angular variation in σ.

In our early experiments (without the vane present) it was noted for certain flow directions that there was an increase in wave amplitude after an initial decay period, following the removal of the electric field. This behaviour was due to the interaction of spurious modes (see Discussion). When the vane, described previously, was used the increase in the amplitude of an initially decaying wave, was eliminated. Damping runs were conducted with different grooved bases as well as with a smooth base. Typical oscilloscope outputs displaying wave amplitude as a function of time are shown in Figure (6-9). In Figures (10-13) the logarithmic plots of wave amplitude as a function of time for the various bases are given. In Figure (14-17) the damping frequency σ is plotted as a function of θ for each base (smooth aluminum base, 33 r.p.m. record with two smooth varnished quadrants, and grooved aluminum plate with two smooth quadrants).

The results for the smooth aluminum base show that the wave tank does not possess any directional damping properties. We also find no sinusoidal variation in σ with θ

Figure 6. Damping runs for a smooth aluminum base (horizontal scale 5 sec/div).

(a) $\theta = 0°$ (vert. 0.2, 0.1 and 0.05 v/div)

(b) $\theta = 45°$ (vert. 0.2, 0.1 and 0.05 v/div)

(c) $\theta = 90°$ (vert. 0.5, 0.2 and 0.1 v/div)

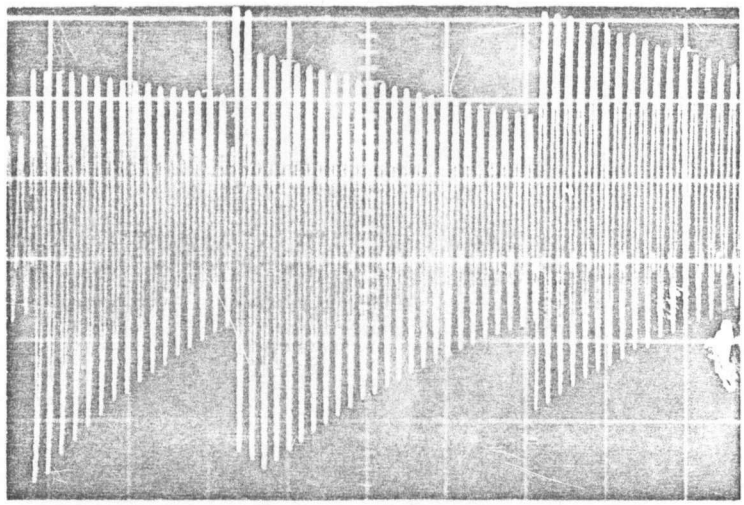

a

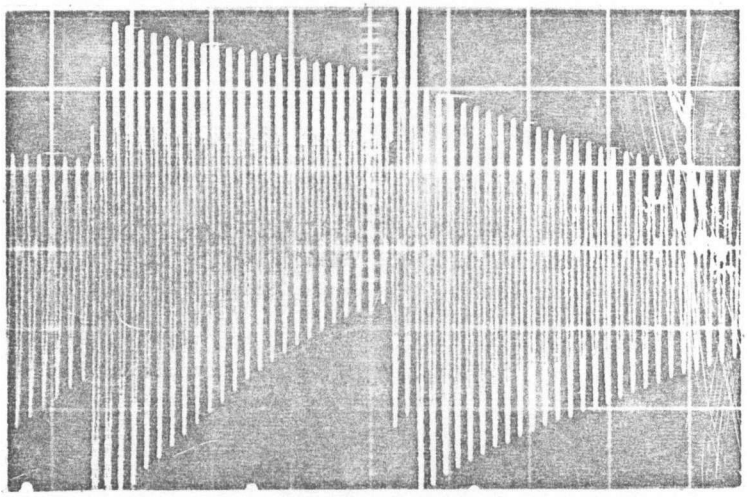

b

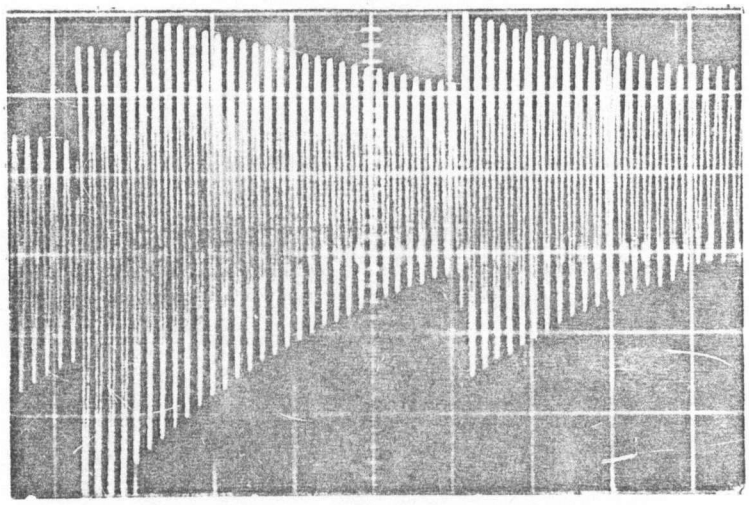

c

Figure 7. Damping runs for a grooved aluminum base (horizontal 5 sec/div).

(a) $\theta = 0°$ (vert. 0.5, 0.2 and 0.1 v/div)

(b) $\theta = 45°$ (vert. 0.5, 0.2 and 0.1 v/div)

(c) $\theta = 90°$ (vert. 0.2, 0.1 and 0.05 v/div)

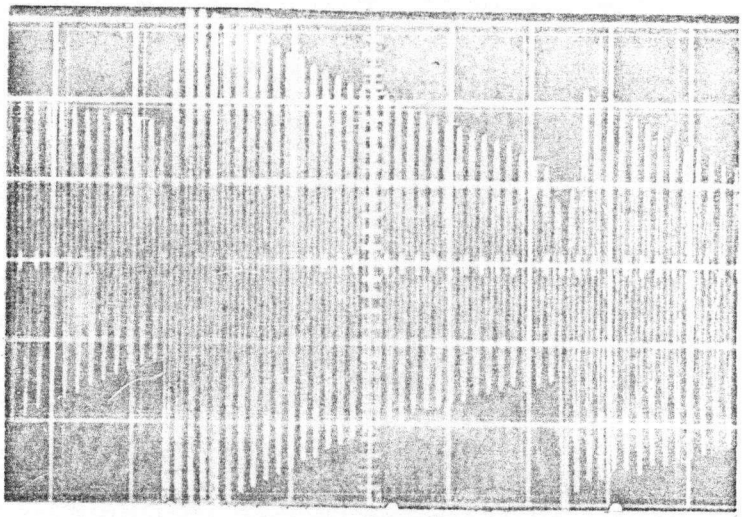

a

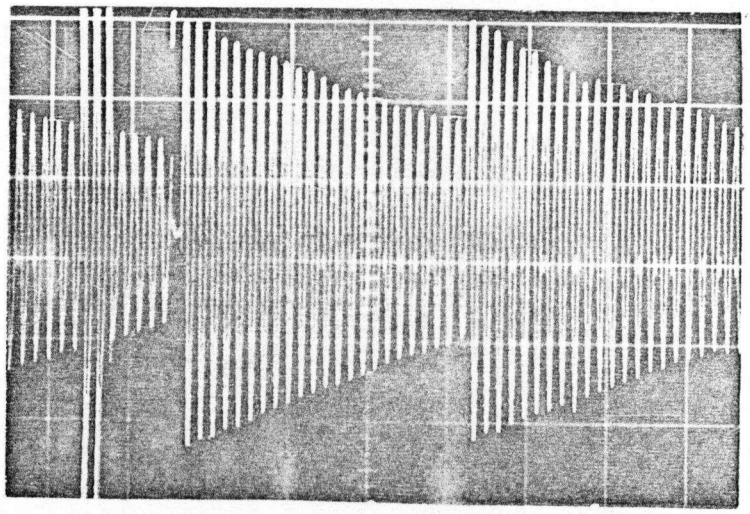

b

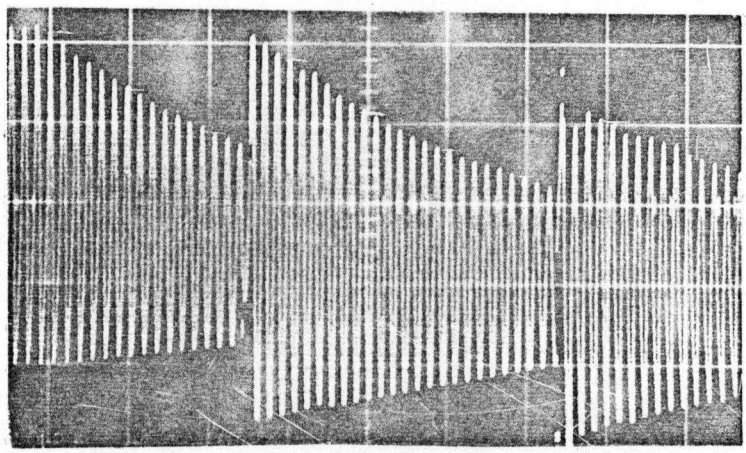

c

Figure 8. Damping runs for 33 r.p.m. record used as a base (horizontal 5 sec/div).

(a) $\theta = 0°$ (vert. 0.2, 0.1, 0.05 v/div)

(b) $\theta = 30°$ (vert. 0.2, 0.1, 0.05 v/div)

(c) $\theta = 60°$ (vert 0.5, 0.2, 0.1, 0.05 v/div)

(d) $\theta = 90°$ (vert. 0.2, 0.1, 0.05 v/div)

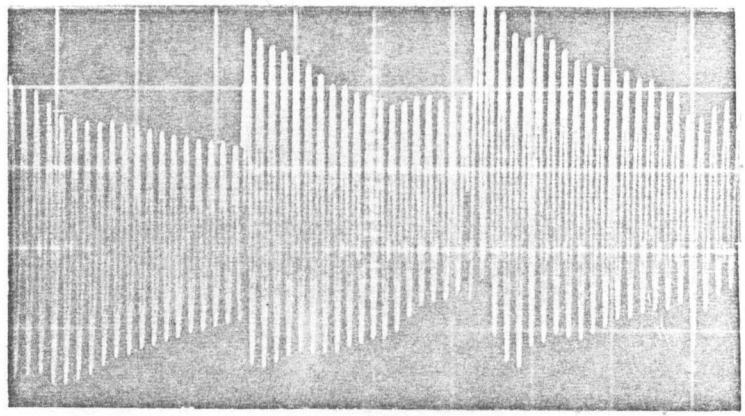

a

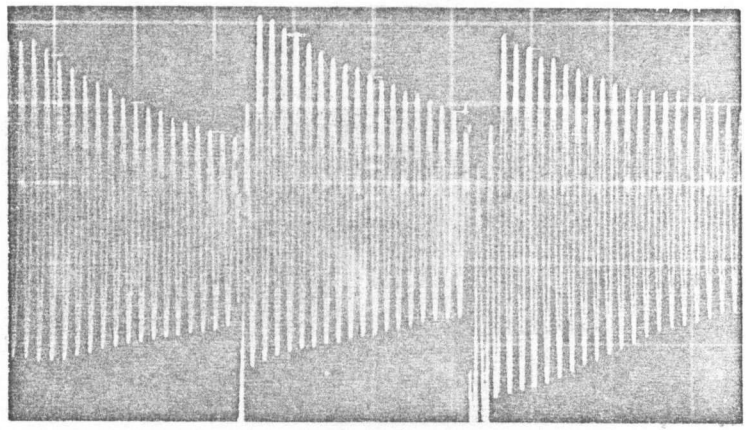

b

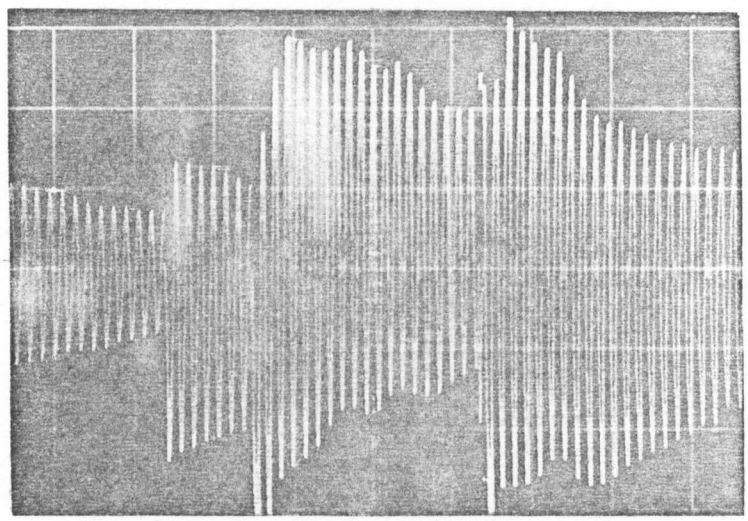

c

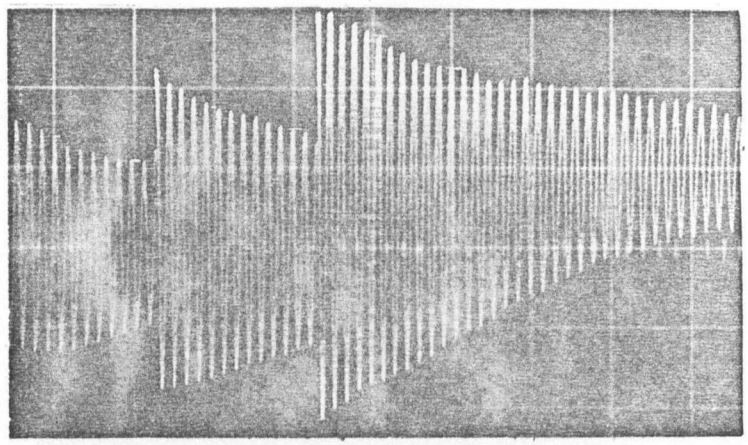

d

Figure 9. Damping runs for a grooved aluminum base (contaminated surface).

(vert. 0.2, 0.1, and 0.05 v/div, horizontal 5 sec/div).

(a) $\theta = 0°$

(b) $\theta = 45°$

(c) $\theta = 90°$

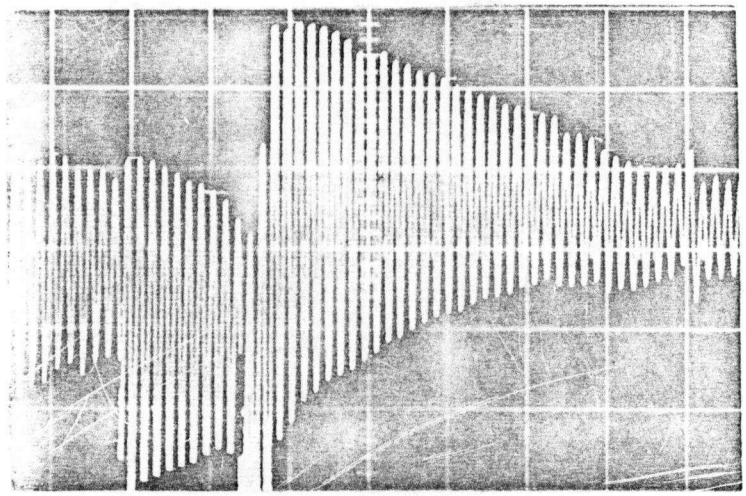

a

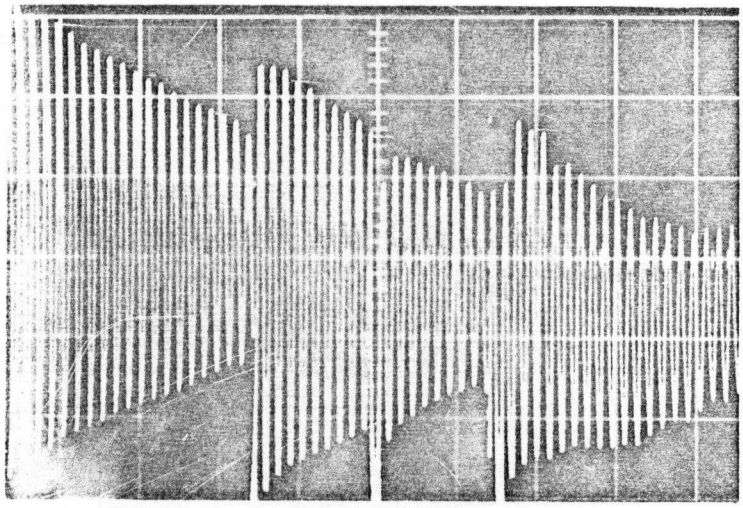

b

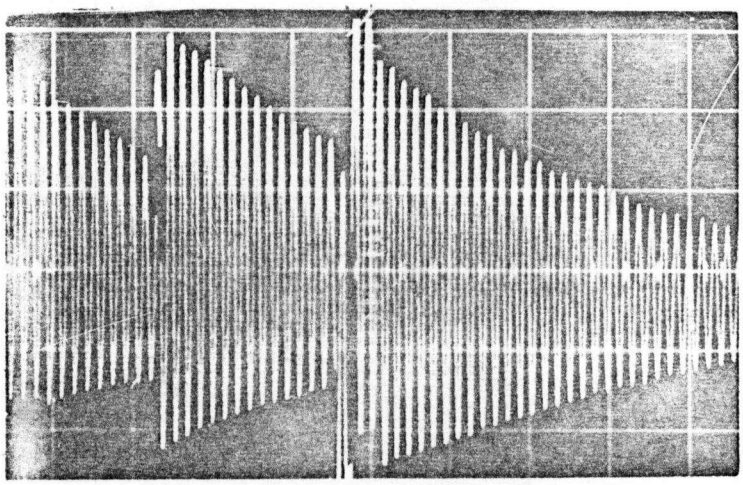

c

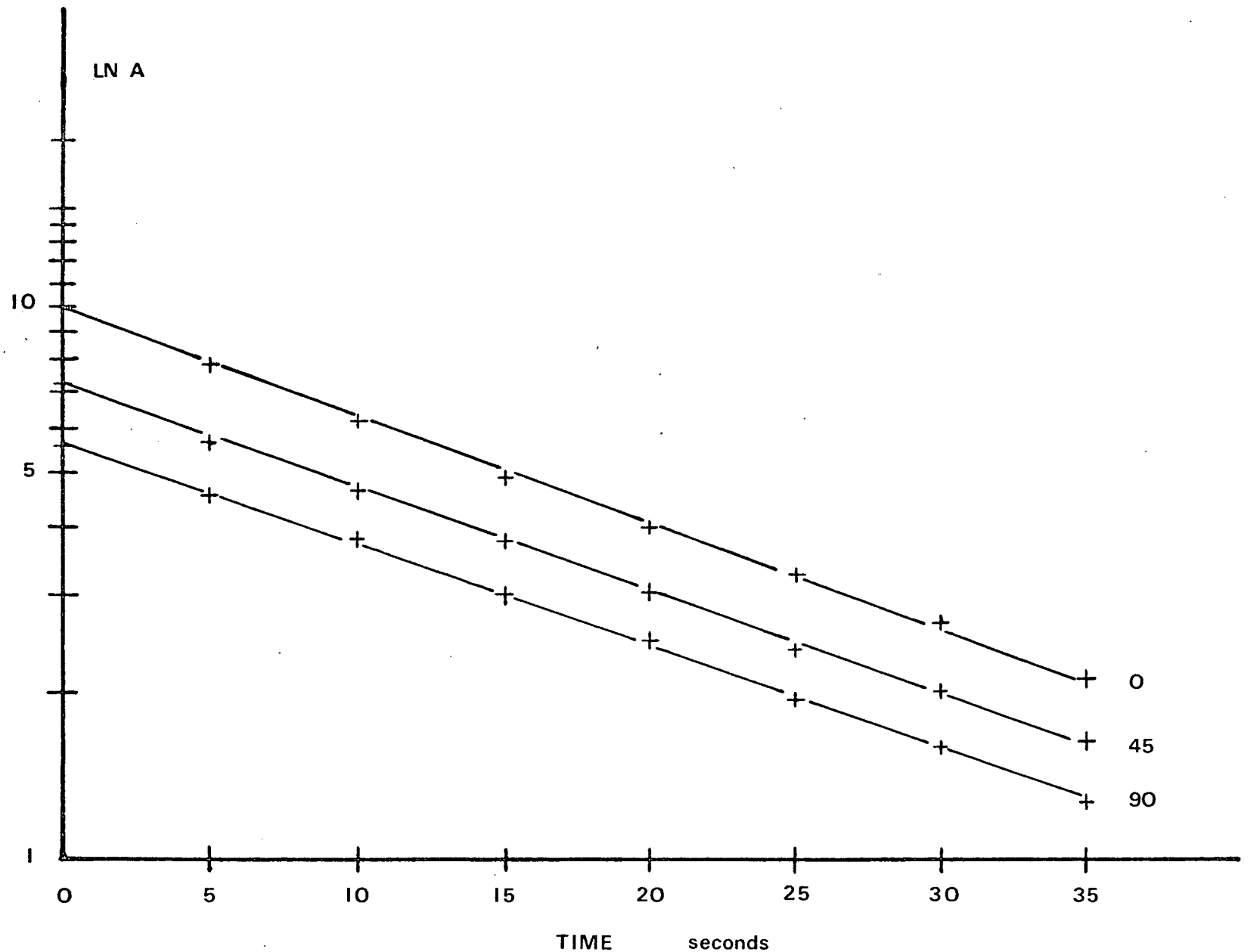

Figure 10. The logarithm of wave amplitude vs time for a smooth base.

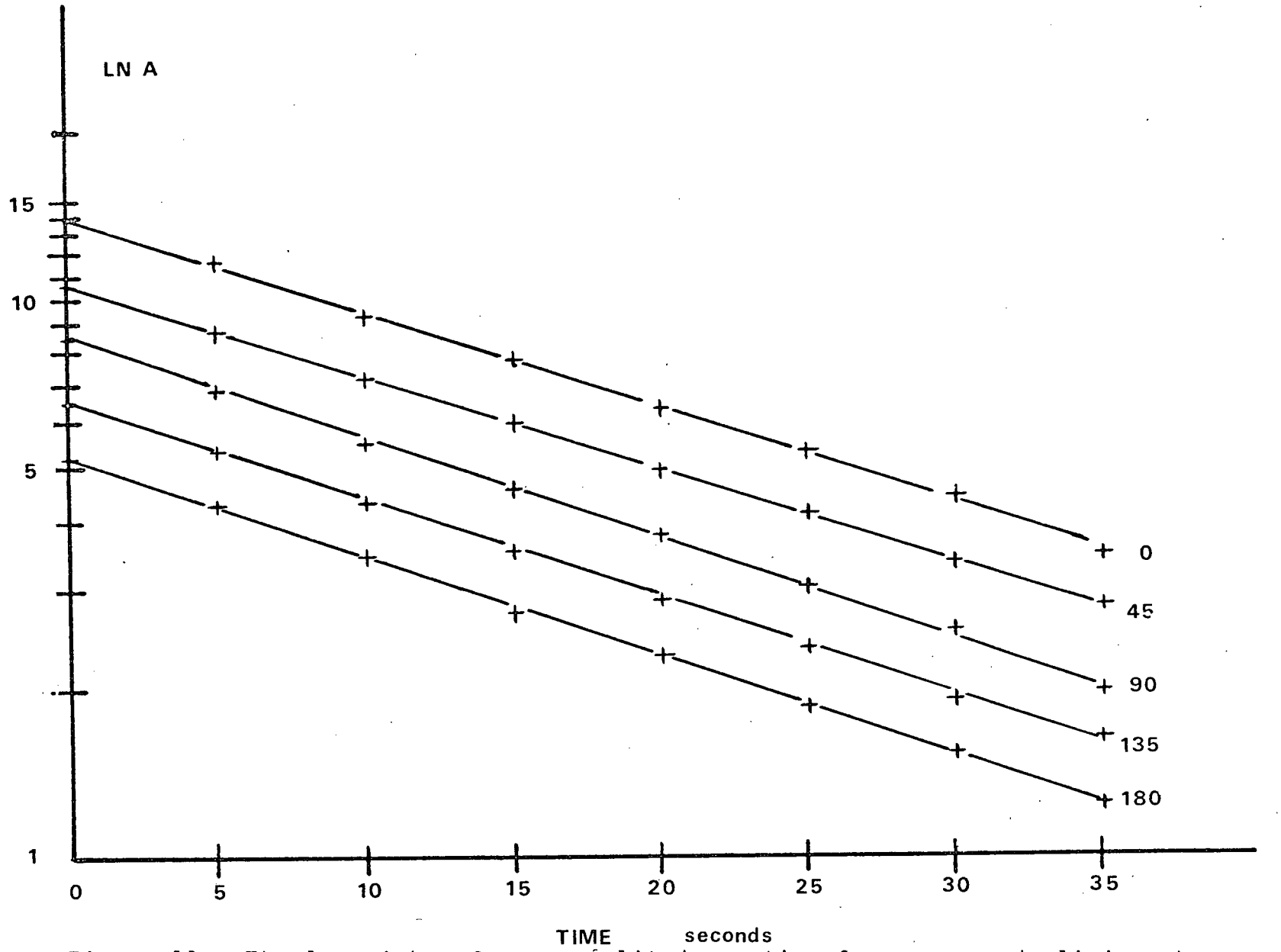

Figure 11. The logarithm of wave amplitude vs time for a grooved aliminum base.

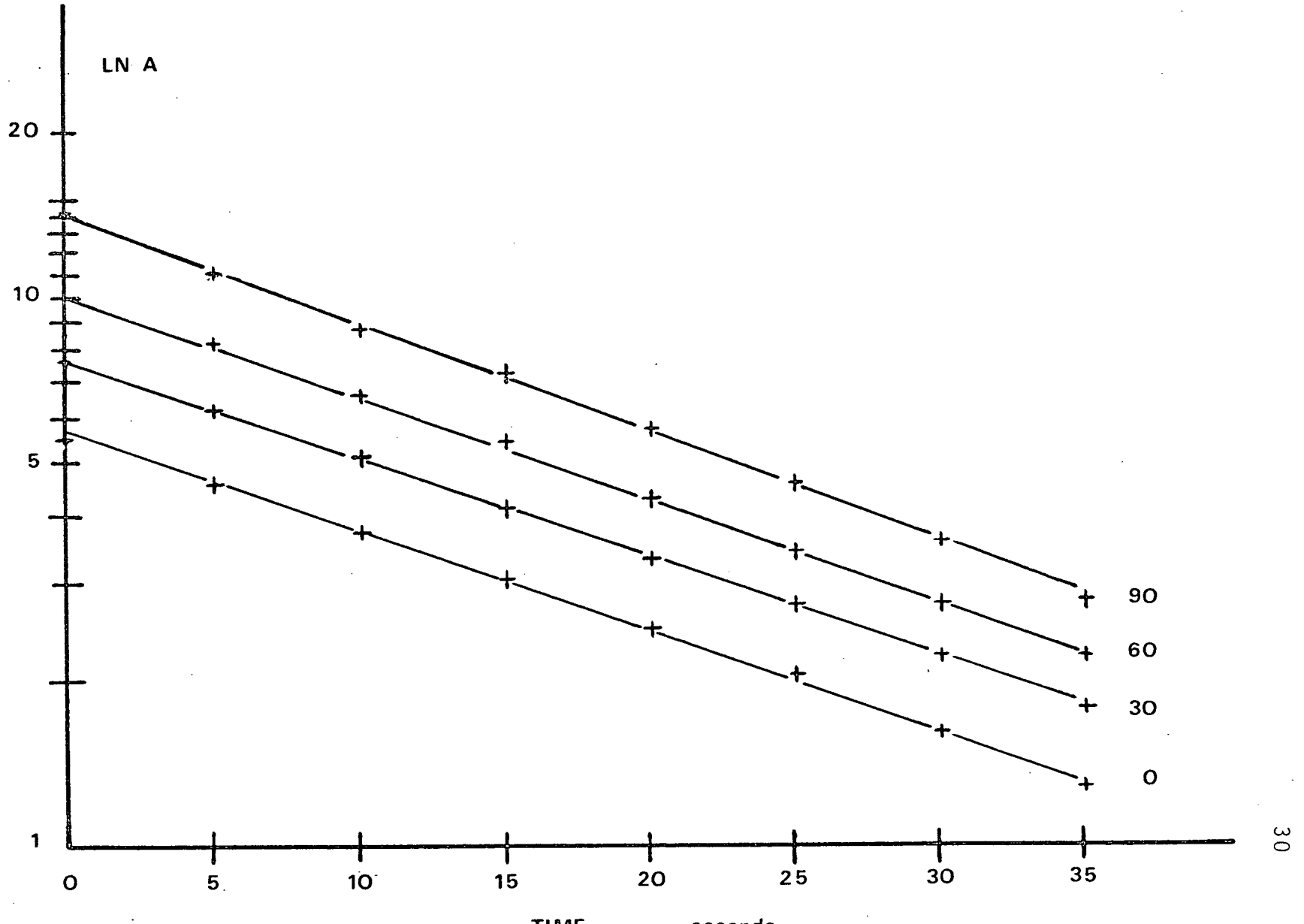

Figure 12. The logarithm of wave amplitude vs time for a 33 r.p.m. record used as a base.

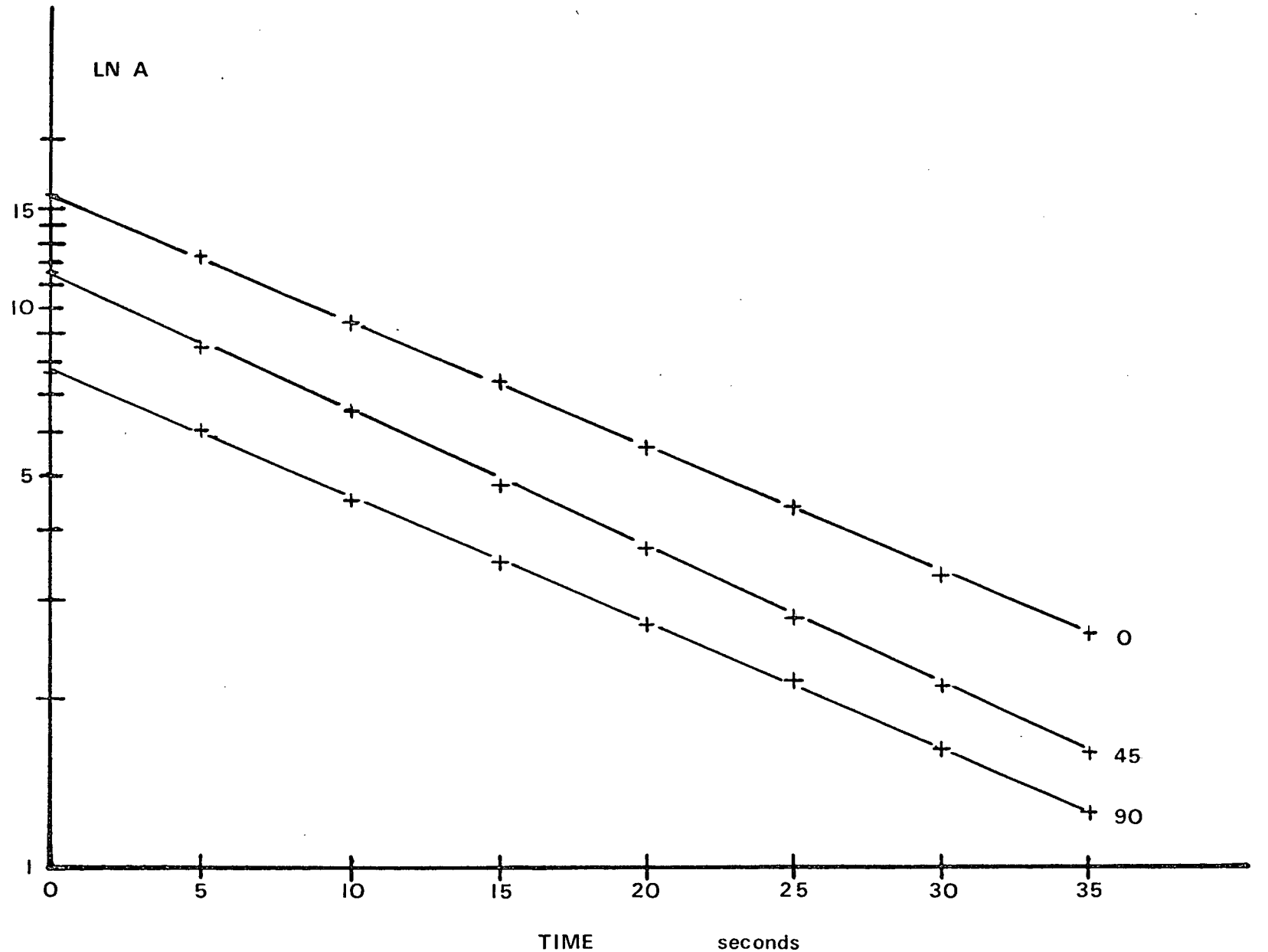

Figure 13. The logarithm of wave amplitude vs time for a grooved aliminum base (contaminated surface).

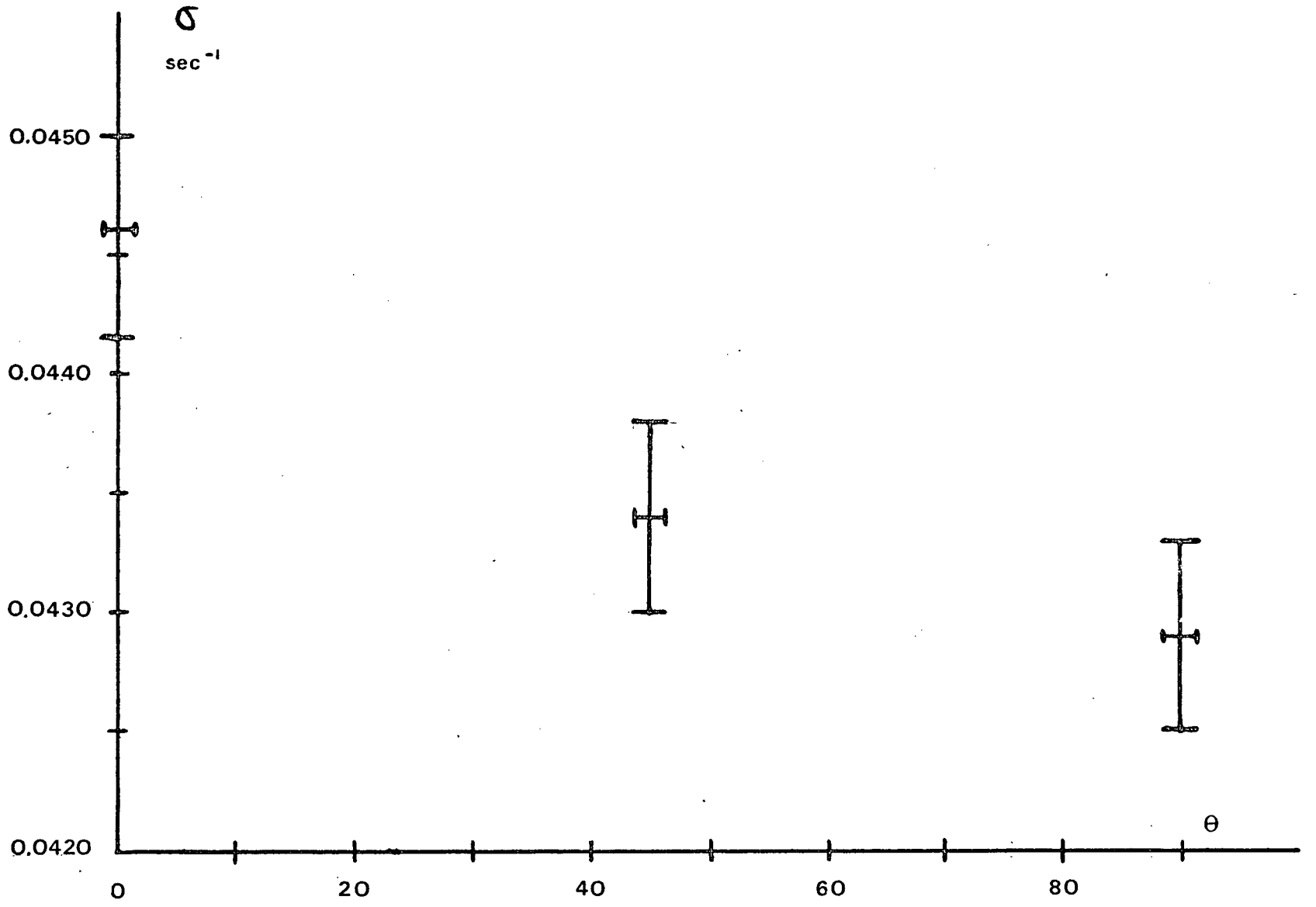

Figure 14. Damping frequence vs θ (smooth base).

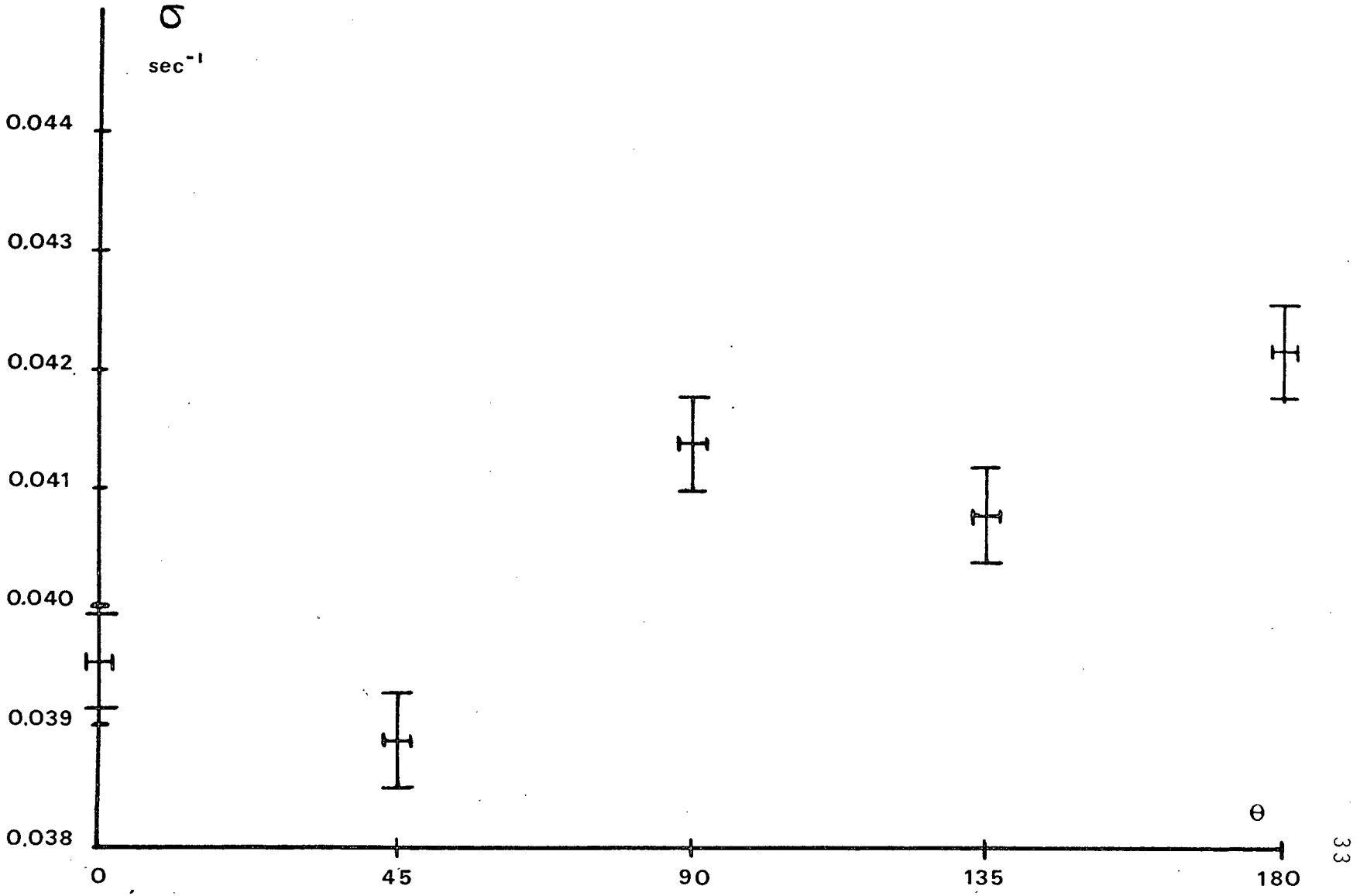

Figure 15. Damping frequency vs θ (grooved aluminum base).

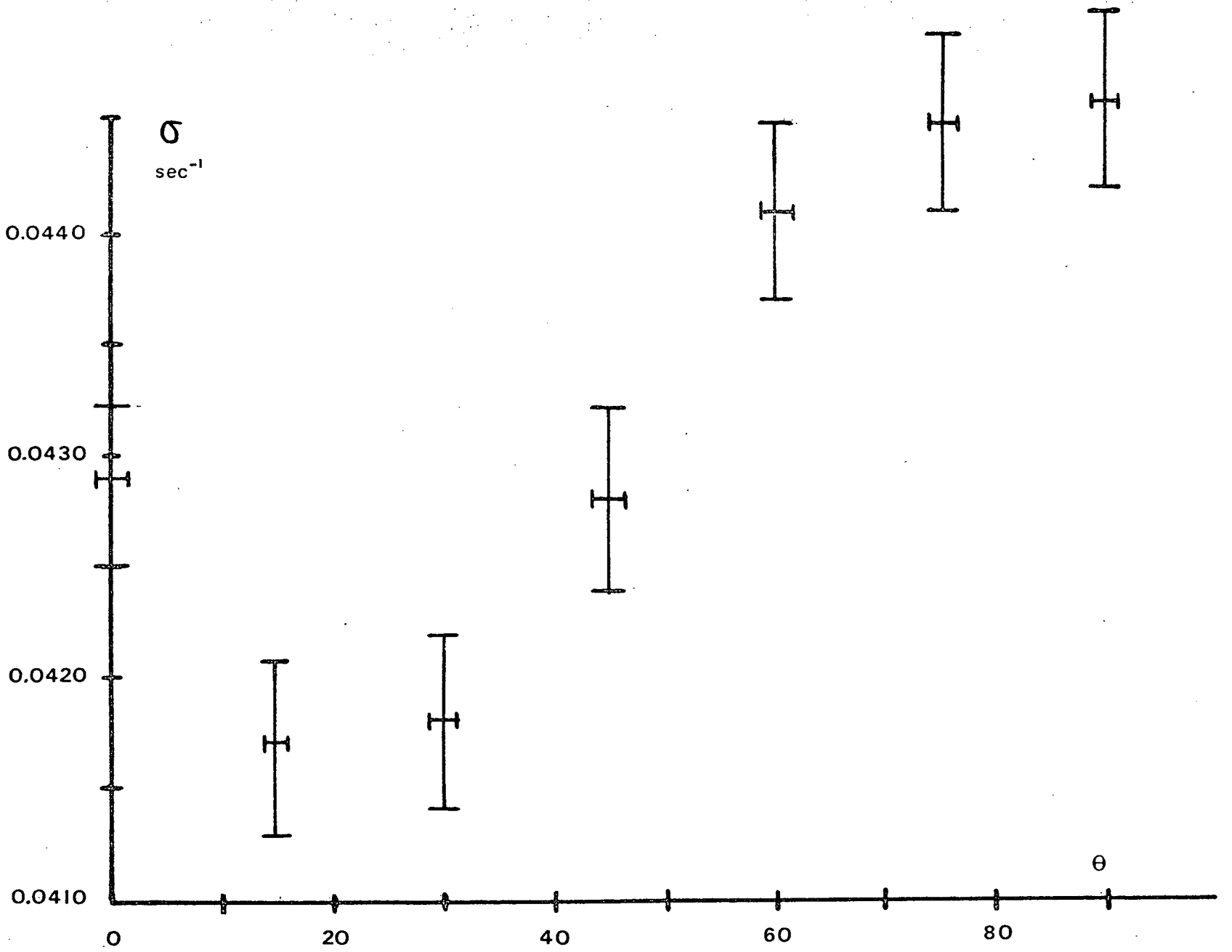

Figure 16. Damping frequency vs θ (33 r.p.m. record used as a base).

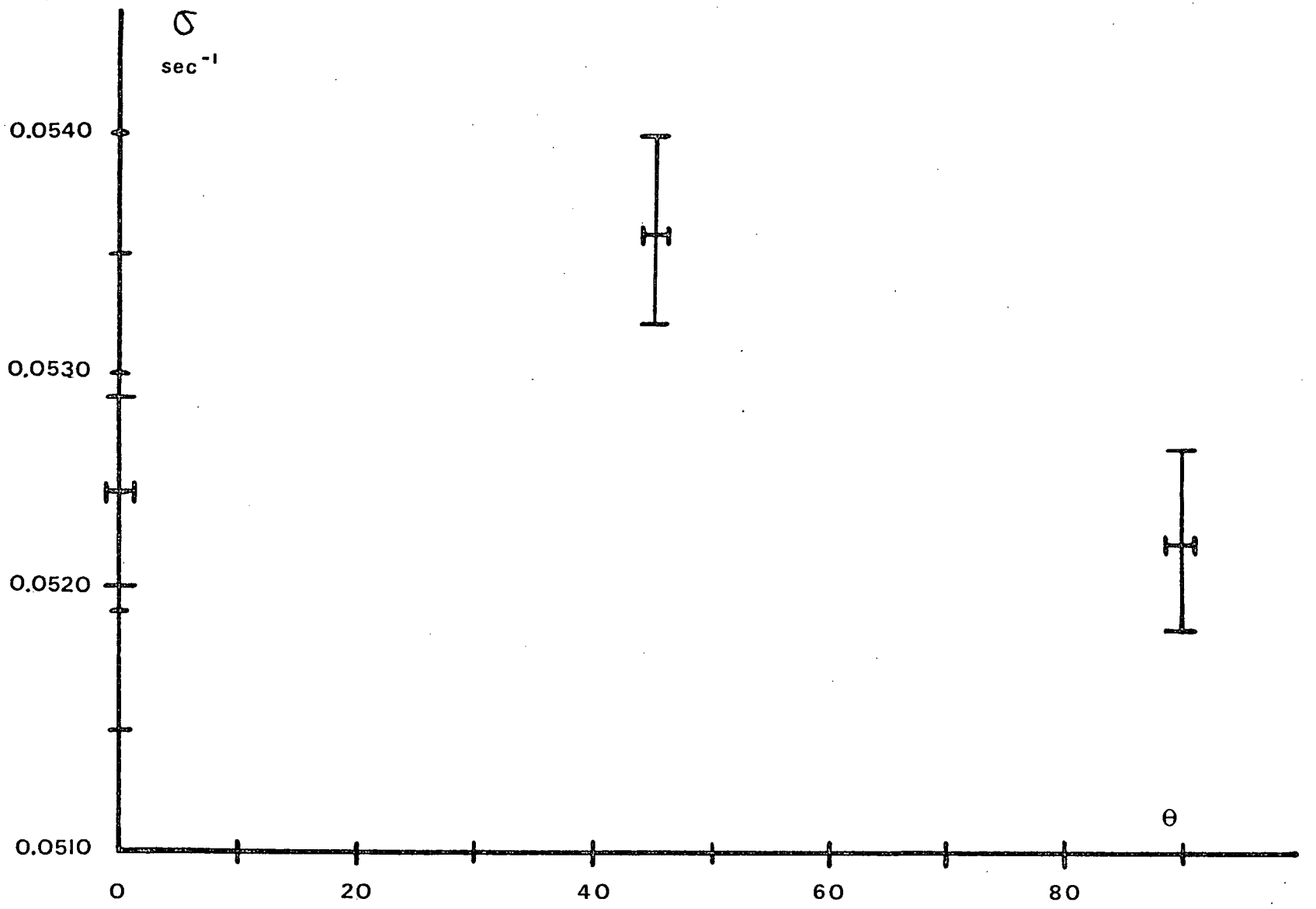

Figure 17. Damping frequency vs θ (grooved aluminum base, contaminated surface).

for the other two grooved bases, as can be seen from Figures (10-13). For both of these bases $a/\ell < 1$, and for this regime we find no significant enhancement in the damping over that for a smooth base, as well as no variation in σ with θ.

The damping frequency as a function of θ for a "dirty" surface using the grooved aluminum plate is shown in Figure (17). The water was left in the tank for a few days and then these damping runs were performed. The magnitude of the damping frequency has increased, but again it exhibits no angular variation.

3.3 Discussion

Case and Parkinson (1957) claim that container "roughness whose depth was small compared to the boundary layer thickness had a remarkably large effect" on the damping of surface waves. They found experimentally values of σ three times larger than that predicted by theory for a dpeth to radius ratio of < 1.5. Case and Parkinson assumed in their theory a laterally mobile surface layer at the air-water interface. With this assumption the energy dissipation in the top surface is negligible compared to that of the base and walls of the tank. In our experiments with a smooth base we found good agreement between experiment and theory,

assuming a laterally immobile top surface. A laterally immobile surface essentially doubles the damping for shallow fluids.

To prepare a laterally mobile top surface requires extreme care and it is reasonable to assume Case and Parkinson did not have such a top surface. This reduces their discrepency between experiment and theory to a factor of 1.5. In our experiments we used depth to radius ratios of 0.2 and we should have certainly seen even larger effects (discrepency between theory and experiment), based on Case and Parkinson's conjecture. Our experimental results do not agree with Case and Parkinson's contention that for shallow fluids surface roughness (even with $a/\ell < 1$) can drastically increase damping.

We found for the grooved bases considered that the variation in damping was only of the order of $< \pm 5\%$ different from that for a smooth base. If Case and Parkinson's contention that surface roughness was responsible for the damping enhancement was valid, then for our model (oppositely grooved quadrants), A' would be equal to 3.

Substituting this in equation (2.8) results in a variation of 20% in σ_2/σ_1, and this variation would be sinusoidal in nature. This variation is much larger than that found in our experiments $\simeq < \pm 7\%$ difference between smooth and groove base results. For both the 33 r.p.m. record and the grooved aluminum plate, σ does not possess

a sinusoidal dependence on θ (see Figures 15-16) as predicted by equation (2.8).

The damping frequency in these runs does possess an angular variation (not sinusoidal in nature), but these variations ($\sim \pm 8\%$) are much smaller than that expected due to Case and Parkinson's conjecture. It was also discovered that there was no systematic behaviour to these variations. Every angular scan of the damping frequency would result in a different angular variation. These variations in σ with θ are, in fact, due to surfactants on the free fluid surface.

As mentioned previously, surfactants make it difficult to establish the effect on wave damping caused by roughened surfaces. The value of the damping frequency was extremely sensitive to the conditions of the distilled water used in the experiments as well as to contaminants present on the grooved base. Variations in σ from day to day, depending on these conditions, were as high as 30%.* While the value of the damping frequency varied for different runs, the damping frequency for any one run did not exhibit any sinusoidal angular dependence. To determine σ as a function of θ ($0° \leq \theta \leq 180°$) takes about one hour and during

---

*It will be noted that the logarithmic plots of wave amplitude versus time are excellent straight lines (as good as those obtained by Ionides. This indicates we are dealing with a single surface mode and we are operating in a regime where linear theory is applicable.

this time fluctuations in the values of σ at any given value of θ are $\sim \leq 5\%$. The damping frequency (determined by least squares fit) has a typical error of less than 1%, so that these variations cannot be explained by the uncertainty of our experimental results. Hence these variations in σ are "real" variations. Since they possess no systematic angular dependence, they cannot be the result of the oppositely grooved quadrants of the base. The variations in σ with θ seen in Figure (14-17), must then be the result of surfactants present on the free surface of the fluid and on the grooved base.

As mentioned previously we observed a spurious dependence of σ on θ in a wave tank where the electrode had no vertical vane under it. For certain values of θ the wave amplitude increased for a certain time after initally decaying, and then finally decreased again to zero. This behaviour is reminiscent of the energy exchange between coupled oscillators having slightly different resonant frequencies, which results in damped beats.

In a wave tank of circular cross-section any sloshing mode can be resolved into two degenerate sloshing modes having their nodal lines perpendicular to each other. However, if the tank is imperfect (slightly elliptical, or with a sloping base), the degeneracy of the two reference modes is removed and they become linearly coupled.

During the driving cycle, the reference modes are constrained such that the nodal line of the fluid surface is near the centre strip of the electorde. However, during the decay phase, energy can be exchanged between the modes because of the coupling. As a result the displacement of the fluid surface exhibits the phenomenon of damped beats. When the damping frequency is higher than the beat frequency it is easy to overlook the existence of the beats and describe the observations in terms of a dependence of σ in θ in a periodic fashion. However, we found that these damped beats could be completely eliminated by the vertical vane under the electrode. The vane constrains the system to oscillate such that the nodal line always remains along a diameter perpendicular to the vane.

3.4 Conclusions

The experimental results for the damping of surface waves in a circular wave tank having a base with alternately grooved quadrants shows that the damping is independent of the direction of the surface mode with respect to the base for groove amplitudes smaller than the boundary layer thickness. On the basis of Case and Parkinson's suggestion, the damping frequency should have possessed an angular variation if the wall roughness did in fact greatly enhance the damping.

We did however observe fluctuations in the damping frequency (~ 30%) from day to day, but on any run there was no systematic angular dependence. These results strongly suggest that this variation in σ is due to surfactants. The roughness of the container walls plays at best only a minor role in the increase of σ. In our experiments we were unable to find any systematic increase in the damping caused by base roughness, where the roughness amplitude is smaller than the viscous boundary layer thickness.

PART B

Chapter 4

4.1 Introduction

From the results of Part A, we found that wall roughness does not significantly increase the damping of surface waves, when the amplitude of the roughness is smaller than the viscous boundary layer thickness. Wall roughness of small dimensions ($a < \ell$) has in the past been conveniently (but erroneously) used to explain discrepancies between theory and experiment. In this section the effect of large grooves ($a >> \ell$) on the damping in a wave channel is examined theoretically and experimentally. The enhancement factor A' used in Section 2.2 is an ad-hoc approach to the problem of damping over roughened surfaces, as it assumes that the flow velocity is unaltered in the dissipation integrals. This might be justified for small groove amplitudes, but not for large grooves. Any meaningful calculation of the damping must involve changes in the flow velocity over the roughness structure. In our theoretical study for large grooves, the

calculation of the damping frequency is approached from this point of view.

In determining the damping over a roughened surface, it is necessary to determine the inviscid velocity potential over the roughness structure (see Section 4.2). The structure of the boundary layer (where essentially all energy dissipation occurs) is then determined by solving the boundary layer equation subject to the boundary conditions that the fluid in contact with the container be at rest.

Roughened container walls change the velocity potential from a value ϕ_0 (the value with smooth walls) to some value ϕ and they change the effective surface area of the boundary layer. There are two approaches to determine the inviscid velocity potential over a roughened surface. A linear perturbation scheme is the most general approach, starting from the smooth wall potential ϕ_0. To do this, the roughness structure is decomposed into Fourier components. The components for which $a(\xi)/\xi > 1$, where $a(\xi)$ is the amplitude of a Fourier component of wavelength ξ will have the greatest effect in changing ϕ_0. The term $a(\xi)/\xi$ is used as an expansion parameter. For the Fourier terms having the greatest effect on changing the potential ϕ_0, the term $a(\xi)/\xi$ is not an appropriate expansion parameter. The perturbation scheme linking ϕ to ϕ_0 for these modes will certainly be nonlinear in the expansion parameter $a(\xi)/\xi$ if $a/\xi = O(1)$. Since

we are interested in large amplitude roughness, a perturbation approach is inappropriate.

An alternative approach is to look for exact solutions to Laplace's equation which satisfy the inviscid flow boundary condition $\underline{n} \cdot \nabla\phi = 0$ on non-flat boundaries for which $a(\xi)/\xi = O(1)$. For this approach it is necessary to know the roughness structure $a(\xi)$ and for any calculation a certain structure is assumed. If there are many grooves (spacing ξ) per wavelength of the surface mode (i.e. $k\xi << 1$ where k is the wave number of the surface mode); then ϕ_0 should essentially be a constant over linear dimensions of order ξ. Above the roughness structure, $\phi - \phi_0$ should decay to zero over vertical length scales of $\sim n\xi$ ($n > 1$), and the particular solution over the grooved structure must incorporate this feature. The term $k\xi$ can then effectively be viewed as an expansion parameter replacing a/ξ. The roughness structure considered in our investigation consists of a surface with identical parallel grooves having a cross section in the shape of an isosceles triangle.

An exact solution for the inviscid velocity potential ϕ for this structure was determined which is valid even if $a(\xi)/\xi > 1$, provided that $k\xi << 1$. The damping was then calculated using ϕ. The results of this calculation show that the energy dissipation in the boundary layer is proportional

to the surface area of the grooved surface, and independent of the orientation of the inviscid* flow with respect to the direction of the grooves.

4.2 Theory

The motion of a viscous fluid is determined from the Navier-Stokes equation. It is assumed in all of our calculations that the fluid we are dealing with is incompressible, i.e. $\nabla \cdot \underline{v} = 0$, where $\underline{v}$ is the fluid velocity. For the fluid used in all of our experiments (water) this is certainly appropriate. In the calculation to follow a right handed cartesian co-ordinate system is used with the xy plane on the undisturbed fluid surface, and the z axis vertically upwards. The linearized Navier-Stokes equation for an incompressible fluid is

$$\frac{\partial \underline{v}}{\partial t} = -\nabla\left(gz + \frac{P}{\rho}\right) + \nu \nabla^2 \underline{v} \qquad (4.1)$$

where P = pressure, ρ = density, and ν is the kinematic viscosity.

The boundary condition for this flow is that

---

*In this case the inviscid flow referred to is measured at several boundary layers above the grooved surface. It is therefore the flow which would remain if the groove amplitude a is decreased to zero.

$$\underline{v} = 0 \tag{4.2}$$

on fixed boundaries. Viscous flow creates the additional constraint that the tangential velocity at fixed boundaries is zero. The decrease of the velocity to zero occurs almost exclusively in a thin layer next to the solid wall. This layer is called the boundary layer and is characterized by the presence in it of considerable velocity gradients. For inviscid flow the only constraint at fixed boundaries is that the normal component of the velocity be zero. For viscous flow the velocity can be written in the form

$$\underline{v} = \nabla\phi + \underline{v_1} \tag{4.3}$$

where $\underline{v_1}$ can be written in terms of a vector potential $\underline{A}$, i.e.

$$\underline{v_1} = \nabla \times \underline{A} \tag{4.4}$$

The first term $\nabla\phi$ is the potential flow term, while the second term $\underline{v_1}$ is the rotational flow term.

Since the flow is incompressible ($\nabla \cdot \underline{v} = 0$) then it follows that

$$\nabla^2\phi = 0 \tag{4.5}$$

Substituting the expression for $\underline{v}$ into the Navier-Stokes equation gives

$$\frac{\partial}{\partial t}(\nabla\phi) + \frac{\partial}{\partial t}(\underline{v_1}) = -\nabla\left(gz + \frac{P}{\rho}\right) + \nu\nabla^2(\nabla\phi + \underline{v_1}) \qquad (4.6)$$

This equation (4.6) is broken down into two equations, one for the viscous flow and one for inviscid flow. In the limit of zero viscosity ν, $\underline{v_1} \to 0$. Equation (4.6) then integrates directly to yield

$$\frac{P}{\rho} + gz = -\frac{\partial\phi}{\partial t} + \text{const.} \qquad (4.7)$$

The above solution (4.7) is also valid for the viscous case if

$$\frac{\partial}{\partial t}(\underline{v_1}) = \nu\,\nabla^2\,\underline{v_1} \qquad (4.8)$$

Equations (4.5) and (4.8) are solved subject to the constraint that the fluid be at rest at rigid boundaries. Expressed mathematically these conditions are

$$\underline{n} \cdot \nabla\phi = 0 \qquad (4.9)$$

$$(\underline{n} \times \nabla\phi) + \underline{n} \times (\underline{\nabla} \times \underline{A}) = 0 \qquad (4.10)$$

where $\underline{n}$ is a unit normal directed inwards from the solid boundary to the fluid. At any rigid boundary the velocity varies rapidly in the direction of $\underline{n}$. All of the other spatial derivatives of the velocity are small compared with variations in the $\underline{n}$ direction. Equation (4.8) can thus be simplified to

$$\frac{\partial}{\partial t}\,(\underline{v_1}) = \nu\,\frac{\partial^2}{\partial \eta^2}\,\underline{v_1} \tag{4.11}$$

The time variation of $\underline{v_1}$ will be assumed to be a simple harmonic time dependence $v_1 \sim e^{i\omega t}$ where ω is the frequency of the surface waves. From (4.11) the solution for v_1 will be of the form

$$v_1 \sim \exp - \left[\eta(1 + i)/\ell\,\sqrt{2}\right] \tag{4.12}$$

where ℓ is the viscous boundary layer thickness $\ell = \left(\frac{\nu}{\omega}\right)^{\frac{1}{2}}$ and η is the co-ordinate along $\underline{n}$. To satisfy the boundary conditions at the wall v_1 must include the term $\nabla\phi$ (Nb. that $\nabla\phi$ in $\underline{v_1}$ does not alter the solution of (4.11) since $\nabla^2\phi = 0$). The complete solution for v_1 is

$$v_1 = \underline{n} \times (\underline{n} \times \nabla\phi) \exp - \left[\eta(1 + i)/\ell\,\sqrt{2}\right] \tag{4.13}$$

where $\nabla\phi$ is evaluated at $\eta = 0$. The viscous energy dissipation per unit area of the container walls is dependent upon v_1, and is given by [see Case and Parkinson]

$$S = -\nu \frac{\partial}{\partial \eta}\left(\frac{1}{2} v_1^2\right)_{\eta=0} = -\nu\left(v_1 \frac{\partial v_1}{\nu \eta}\right)_{\eta=0} = \nu\left(\nabla\phi\right)^2_{\eta=0} / \ell \sqrt{2} \qquad (4.14)$$

It was remarked earlier that the energy dissipation is only dependent on the inviscid velocity potential, and this can be seen to be the case from (4.14). To determine the damping it is necessary to integrate S over the container surfaces; the damping frequency is then proportional to $\int S dA$. Hence the effects of a roughened surface on the damping can be determined by calculating $\int S dA$. To do this it is necessary to evaluate the inviscid velocity potential over the roughness structure (grooved structure). The inviscid potential for two groove cross sections (triangular and approximately sinusoidal) as well as the dissipation integrals for each, are now calculated. In the following calculations it is assumed that the boundary layer thickness ℓ is much smaller than any other scale lengths of the problem and there are many grooves (spacing ξ) per wavelength of the waves (λ).

For a flat surface the energy dissipation $S = S_0$ where

$$S_0 = \nu v_0^2 / \ell \sqrt{2} \qquad (4.15)$$

and v_0 is the inviscid flow velocity parallel to the surface. If fluid flows parallel to the grooves, v_0 is unaltered by the grooves but the boundary layer spreads over the grooved surface (see Figure 19(b)) increasing the dissipation area from dA_0 to dA (dA_0 is an element of area on the flat surface, dA is over the grooved surface. Hence for flow parallel to the grooves the dissipation is increased in the ratio dA/dA_0.

For flow transverse to the grooves, v is changed. At the top of the grooves $v > v_0$ and at the bottom $v < v_0$ where in this case v_0 is the inviscid velocity some distance above the grooves. Hence it is not clear what relation SdA bears to $S_0\ dA_0$ as the groove depth is changed.

4.3 Calculation of $\int SdA$ for Grooved Surfaces

When determining the velocity potential over a grooved surface it is convenient to consider a complex velocity potential. The modulus and argument of a complex potential will give the magnitude of the velocity and the angle between the flow direction and in our case the xy plane. For inviscid flow past a solid surface, the velocity must be along the tangent to the surface. Hence the profile of the surface must be the profile of a streamline. For the grooved structures considered a streamline follows the groove structure, which makes it difficult to determine the potential. For all

of our calculations the groove structure is considered to be in the complex z-plane. If it is possible to determine a transformation which maps the groove structure in the z-plane onto the real axis of the w-plane, then the problem is greatly simplified. The streamlines of the flow in the w-plane will thus be straight lines parallel to the real axis. The problem of flow past a given contour then reduces to the determination of an analytic function w(z) which takes real values on the contour. With this approach it is possible to determine the potential over the grooved structure and thus the dissipation integrals can be solved.

Consider $\phi = w = f(z)$ to be the complex velocity potential transverse to the grooves. The magnitude of the speed u at the grooved surface is then given by

$$u = \mu|\nabla\phi| = \mu\left|\frac{dw}{dz}\right| \tag{4.16}$$

This velocity potential must have the property that far above the groove structure, their effect is negligible, i.e. $u \to v_0$ as $Im(z) \to \infty$. The constant μ is chosen so that this is the case. Using (4.16) in the dissipation integral results in

$$\int SdA = \left(\frac{\nu}{\sqrt{2}\ \ell}\right) \mu^2 \int \left|\frac{dw}{dz}\right|^2 |dz||dL| \qquad (4.17)$$

where dL is a length element on a groove over the area being considered. The integral over dz is along the groove structure. As stated previously, the evaluation of this integral is simplified if the groove structure is mapped into the real axis of the w-plane. Then the line integral over dz transforms to a line integral over dw. For this (4.17) can be written in a more convenient form.

$$\int SdA = \mu^2 \left(\frac{\nu}{\sqrt{2}\ \ell}\right) \int \left|\frac{dw}{dz}\right| |dw| \qquad (4.18)$$

The case of grooves with a cross section in the form of an isosceles triangle is first considered (see Figure 19a). To determine the potential and dissipation integral for this case, a transformation mapping the groove structure into the real axis of the w-plane is required. It is well known that the interior of any polygon D in the z-plane can be mapped into the upper half D' of the w-plane by a Schwartz-Christoffel transformation (see Figure 18a).

The most general form of the Schwartz-Christoffel transformation is

$$\frac{dz}{dw} = A(w-w_1)^{\alpha_1/\pi-1} \quad (w-w_2)^{\alpha_2/\pi-1} \cdots (w-w_n)^{\alpha_n/\pi-1} \qquad (4.19)$$

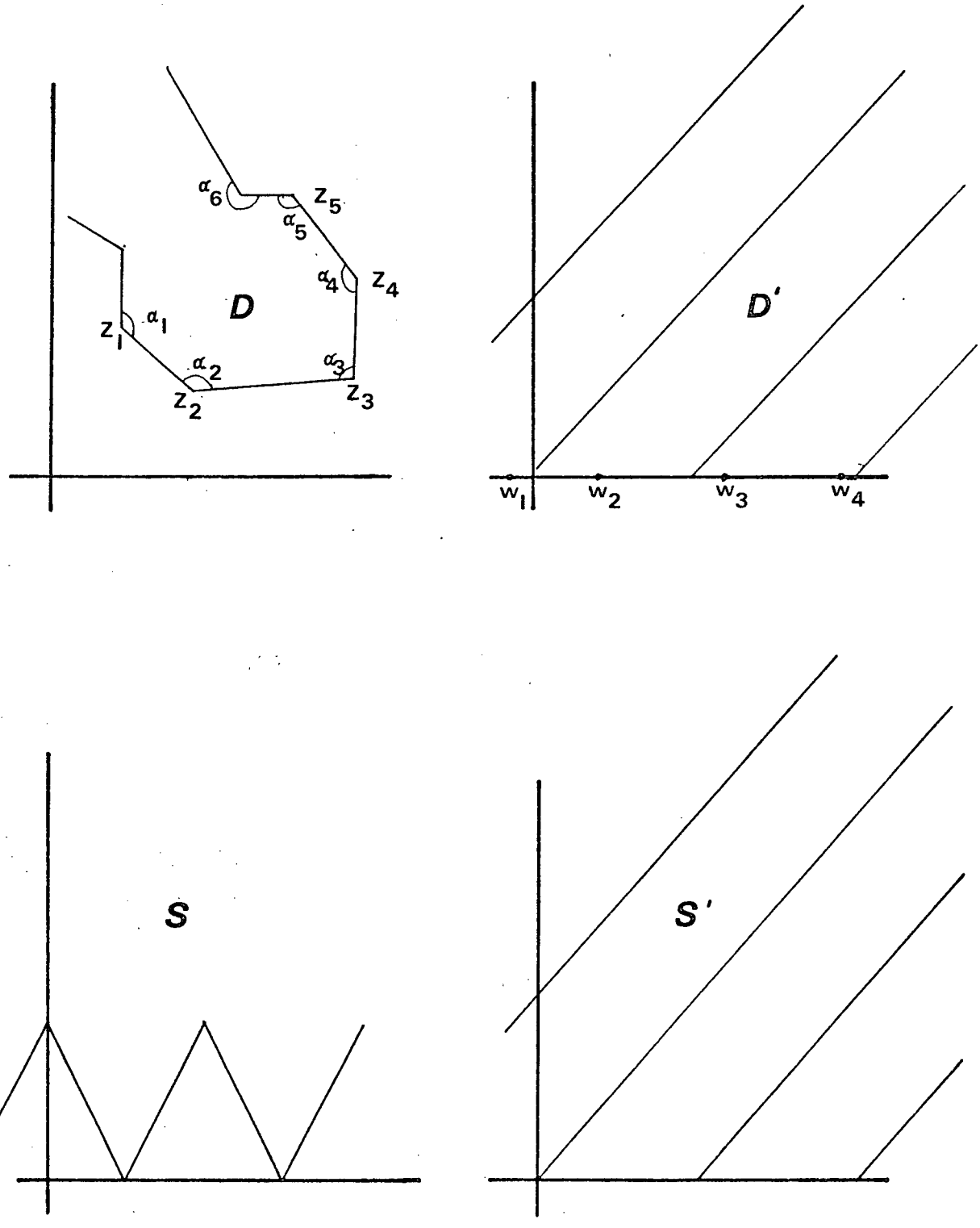

Figure 18. Mapping of a polygonal region into the upper half of the w-plane.
(a) Arbitrary polygonal region.
(b) Region bounded by a triangular groove structure.

and this can be used for polygonal regions with vertices at ∞. Thus it is possible to map region S bounded by a grooved structure into the upper half plane S' (Figure 18b). The groove structure that has been considered can be viewed as a superposition of individual triangles.

The Schwartz-Christoffel transformation for a single triangle is first calculated. The points $z = -b, ai, +b$ are mapped into the points $w = -1, 0, +1$ respectively in the w plane (Figure 19a). Then

$$\frac{dz}{dw} = A(w+1)^{\pi-\alpha/\pi-1}\, w^{\left(\frac{\pi+2\alpha}{\pi} - 1\right)}\, (w-1)^{\pi-\alpha/\pi-1}$$

$$= A(w^2-1)^{(\pi-\alpha/\pi) - 1}\, w^{(\pi+2\alpha/\pi) - 1}$$

$$= \frac{A\, w^{2\alpha/\pi}}{(w^2-1)^{\alpha/\pi}} \equiv \frac{K\, w^{2\alpha/\pi}}{(1-w^2)^{\alpha/\pi}} \qquad (4.20)$$

The constant K is chosen to fix the length of one side of the isosceles triangle. Integrating (4.19) yields

Figure 19: Features of the groove geometry.

(a) Mapping contours for the velocity potential.

(b) Flow of water along the grooves.

(c) Geometry of grooved area dA, with p grooves per unit length (p = 3 in Figure 19c).

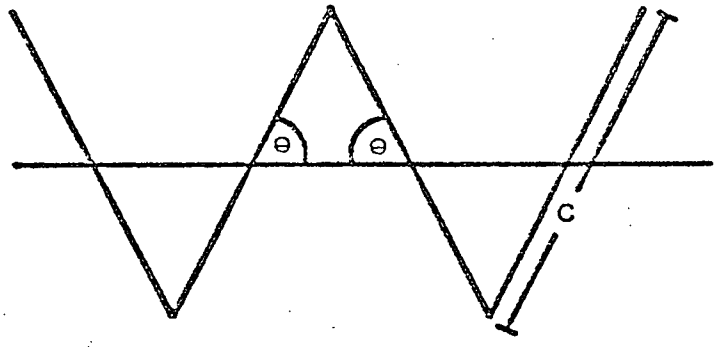

z-plane

(a)

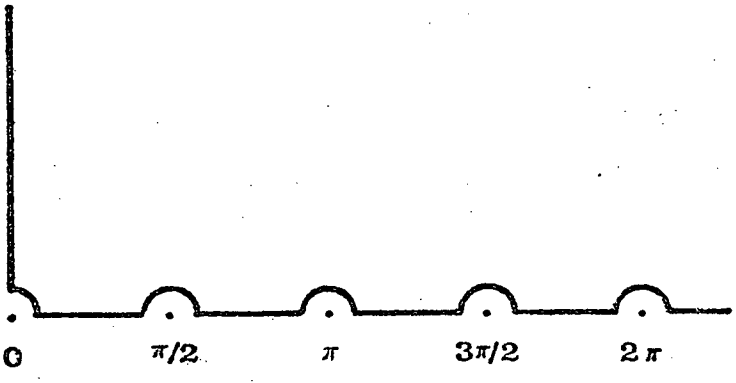

w-plane

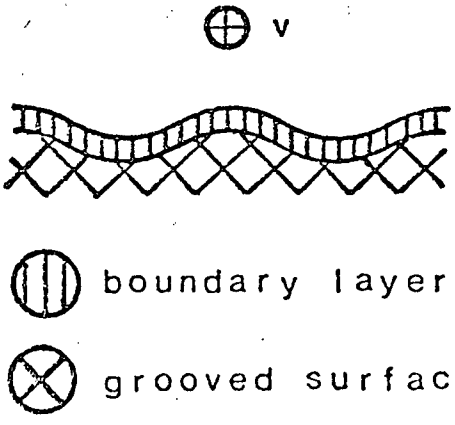

(b)

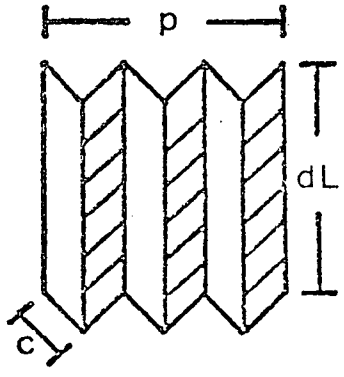

(c)

$$z = K \int_0^w \frac{\psi^{2\alpha\pi}}{(1 - \psi^2)^{\alpha/\pi}} \, d\psi + B \tag{4.21}$$

For $w = 0$, $z = ai$ and for $w = 1$, $z = b$. Using this, K is given by

$$K = \frac{b - ai}{\int_0^1 \frac{\psi^{2\alpha/\pi} \, d\psi}{(1 - \psi^2)^{\alpha/\pi}}} \tag{4.22}$$

The S-C Transformation for the complete groove structure is calculated in a similar manner to that for a single triangle. The transformation is calculated so that it maps vertices at height ai into $0, \pm 2(\frac{\pi}{2}), \pm 4(\frac{\pi}{2}), \cdots$ and maps vertices on the real axis into $\pm \frac{\pi}{2}, \pm \frac{3\pi}{2}, \cdots$ (see Figure 19a) where $\pi - 2\theta$ is the apex angle of the grooves.

The SC transformation for this is the infinite product

$$\frac{dw}{dz} = A \cdots (w-\pi)^{\frac{\pi+2\theta}{\pi}-1} \quad (w-\pi/2)^{\frac{\pi-2\theta}{\pi}-1} \quad w^{2\theta/\pi} \quad (w+\frac{\pi}{2})^{\frac{\pi-2\theta}{\pi}-1} \cdots$$

$$= \frac{A\, w^{2\theta/\pi}\left[\left(w^2 - 4(\frac{\pi}{2})^2\right)\left(w^2 - 16(\frac{\pi}{2})^2\right)\left(w^2 - 36(\frac{\pi}{2})^2\right) \cdots\right]^{2\theta/\pi}}{\left[\left(w^2 - (\frac{\pi}{2})^2\right)\left(w^2 - 9(\frac{\pi}{2})^2\right)\left(w^2 - 25(\frac{\pi}{2})^2\right) \cdots\right]^{2\theta/\pi}}$$

$$= \frac{K\left[w \prod_{n=1}^{\infty}\left(1 - \frac{w^2}{n^2\pi^2}\right)\right]^{2\theta/\pi}}{\left[\prod_{n=1}^{\infty}\left(1 - \frac{4w^2}{(2n-1)^2\pi^2}\right)\right]^{2\theta/\pi}} \qquad (4.23)$$

Here K is a constant, K = A const. = AC. The constant C results from the factoring of the bracketed terms in the second form of (4.23) which enables the S.C. transformation to be expressed in the final simple form.

Now sin w and cos w have the following infinite product representations [see Abramswitz and Stegun].

$$\sin w = w \prod_{n=1}^{\infty}\left(1 - \frac{w^2}{n^2\pi^2}\right)$$

$$\cos w = \prod_{n=1}^{\infty}\left(1 - \frac{4w^2}{(2n-1)^2\pi^2}\right) \qquad (4.24)$$

Thus (4.23) becomes

$$\frac{dz}{dw} = K\ (\tan w)^{2\theta/\pi} \tag{4.25}$$

The constant K is determined in the same way as for the single triangle case done previously. Integrating (4.25) results in

$$z = \int_0^W (\tan \chi)^{2\theta/\pi}\, d\chi + B \tag{4.26}$$

For W = 0, z = ai so that B = ai, and for W = $\pi/2$, Z = b. Thus K is given by

$$K = \frac{b - ai}{\int_0^{\pi/2} (\tan w)^{2\theta/\pi}\, dw} \tag{4.27}$$

The constant μ (equation (4.16) can now be determined using the condition $u \to v_0$ as $\mathrm{Im}(z) \to \infty$. This requires that

$$\lim_{(\mathrm{Im}\ z \to \infty)} \mu \frac{1}{K(\tan w)^{2\theta/\pi}} = v_0 \tag{4.28}$$

and clearly $\mu = K v_0$.

Now the dissipation integral can be calculated. This integral is calculated over the length of one side of

an isosceles triangle. Due to the symmetry of the groove structure, the dissipation over any one side is equivalent to any other. The total dissipation in length dx will then be 2p times the dissipation for a single side of the isosceles triangle, where p is the number of grooves traversed in a distance dx across the grooves (see Figure 19c). In the w-plane integrating over one side of a groove is equivalent to integrating over the range (0 - $\pi/2$). Now substituting (4.25), (4.27), and (4.28) into (4.18) results in

$$\int SdA = \frac{2p\left(\frac{\nu}{\sqrt{2}\ \ell}\right) v_0^2\ c\ dL \int_0^{\pi/2} (\cot w)^{2\theta/\pi}\ dw}{\int_0^{\pi/2} (\tan w)^{2\theta/\pi}\ dw} \qquad (4.29)$$

where $c = (a^2 + b^2)^{\frac{1}{2}}$.

Now the general form for a Beta Function [Abramowitz and Stegun, 1965] is

$$B(m,n) = 2 \int_0^{\pi/2} (\sin t)^{2m-1}\ (\cos t)^{2n-1}\ dt \qquad (4.30)$$

Hence $$\int_0^{\pi/2} (\cot w)^{2\theta/\pi}\ dw = B\left(\frac{1}{2} - \frac{\theta}{\pi},\ \frac{1}{2} + \frac{\theta}{\pi}\right)$$

$$\int_0^{\pi/2} (\tan w)^{2\theta/\pi}\ dw = B\left(\frac{1}{2} + \frac{\theta}{\pi},\ \frac{1}{2} - \frac{\theta}{\pi}\right)$$

The beta-function is symmetric in its argument, [B(m,n) = B(n,m)] so that (4.29) reduces to

$$\int SdA = \left(\frac{\sqrt{2}\,\nu}{\ell}\right) v_0^2\ p\ c\ dL = 2S_0\ p\ c\ dL \qquad (4.31)$$

But 2 p c dL = dA (see Figure 19c). Hence for flow transverse to the grooves.

$$SdA = S_0\ d\ A_0\ \left(\frac{d\ A}{d\ A_0}\right) \qquad (4.32)$$

The dissipation is thus increased in the ratio dA/dA_0 compared to the dissipation expected for a flat surface. This result is the same as for flow parallel to the grooves as was discussed previously. Hence for a roughened surface with grooves consisting of identical isosceles triangles the dissipation is proportional to the expression $S_0\left(\frac{dA}{d\ A_0}\right) d\ A_0$ irrespective of the direction of the flow with respect to the grooves.

The streamlines above the triangular groove structure have an approximately sinusoidal shape. For a groove structure of this form, the streamline at the groove surface would of course be sinusoidal. Using the transformation (4.25) along the line Im(w) = Y generates a groove structure in the z-plane with an approximately sinusoidal cross section. For this type of structure the dissipation integral becomes

$$\int SdA = \left(\frac{\nu}{\ell}\right) v_0^2 \, p \, K \, dL \int_0^{\pi} |\cot(x + iy)|^{2\theta/\pi} \, dx \qquad (4.33)$$

where $w = x + iy$.

The integral in (4.33) can be written in the form

$$I = \int_0^{\pi/2} \left(|\cot(x + iy)|^{2\theta/\pi} + |\cot(x + iy)|^{-\frac{2\theta}{\pi}} \right) dx \qquad (4.34)$$

using the identity

$$\cot\left(x + \frac{\pi}{2}\right) = - \tan x \qquad (4.35)$$

The arc length for such a groove structure is given by

$$c' = \int \left|\frac{dz}{dw}\right| dw = K \int_0^{\pi} \cot(x + iy)|^{-2\theta/\pi} \, dx \qquad (4.36)$$

The integral in (4.36), however, is the same as (4.34), which can be seen using (4.35). Thus equation (4.36) reduces to

$$c' = KI \qquad (4.37)$$

The dissipation integral is then

$$\int SdA = \left(\frac{\nu}{\sqrt{2}\,\ell}\right) v_0^2 \, p \, dL \, c' = \int S_0 \, dA = \int S_0 \, d \, A_0 \left(\frac{d \, A}{d \, A_0}\right) \qquad (4.38)$$

Hence for a groove structure of approximately sinusoidal cross-section the damping is enhanced in the ratio $\frac{dA}{d\,A_0}$ with respect to a flat surface; and the damping enhancement is independent of flow direction with respect to the grooves.

4.4 Calculation of the Damping Frequency σ

It has been shown previously that the damping (and hence the damping frequency) for surface waves is proportional to $\int S dA$ integrated over the container surfaces. The complete expression for the damping frequency σ is given by

$$\sigma = \frac{1}{2}\left(\frac{\omega\nu}{2}\right)^{\frac{1}{2}}\left[\frac{\int(\nabla\phi)_T^2\, dA}{\int(\nabla\phi)^2\, d\tau}\right] + (S_F) \qquad (4.39)$$

where $(\nabla\phi)_T$ is the tangential inviscid velocity, dA is an element of area on the interface between the water and the wave tank, $d\tau$ is a volume element in the fluid and S_F allows for energy dissipation at the air-water interface. (This result is derived in Appendix A).

Using (4.39) the damping frequency for a square wave tank of length L and depth H with a grooved base is now calculated. The bottom of the tank is at z = -H while the equilibrium fluid surface is at z = 0 (see Figure 20).

The inviscid velocity potential for flow parallel to a pair of vertical walls in the wave tank is [see Landau and Liftshitz].

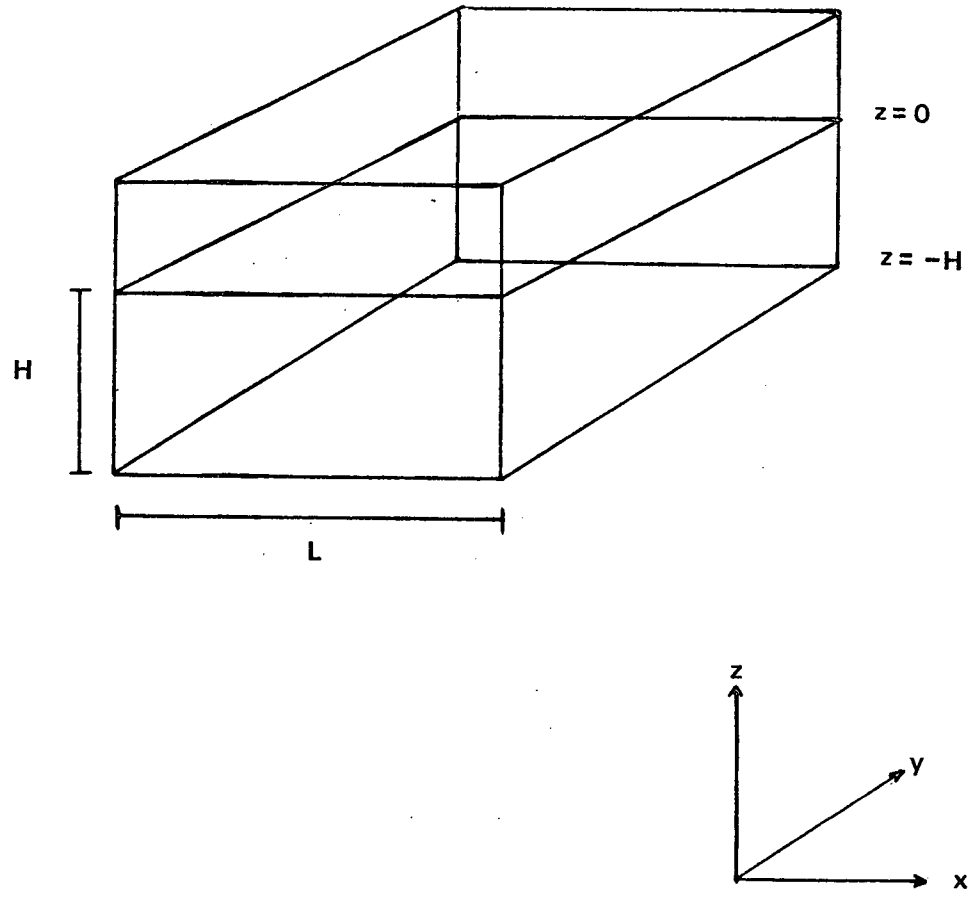

Figure 20. Coordinate system used for the calculation of the damping frequency.

$$\phi = A \cosh k(z + H) \cos kx \cos \omega t \tag{4.40}$$

and

$$v_x = \frac{\partial \phi}{\partial x} = - \frac{A}{k} \sin kx \cosh k(z + H) \cos \omega t$$

$$v_z = \frac{\partial \phi}{\partial z} = \frac{A}{k} \sinh k(z + H) \cos kx \cos \omega t$$

$$A/k \equiv A_1 \tag{4.41}$$

Using these results the integrals in (4.39) can now be calculated, where the integrals are averaged over one oscillation period of the water wave. Now

$$\int (\nabla \phi)^2 \, d\tau = \frac{L^2 A_1^2}{4} \int \cosh^2 k(z + H) \, dz$$

$$+ \frac{L^2 A_1^2}{4} \int \sinh^2 k(z + H) \, dz$$

$$= \frac{L^2 A_1^2}{4} \int_{-H}^{0} \cosh 2k(z + H)$$

$$= \frac{L^2 A_1^2}{4} \left(\frac{\sinh 2kH}{2k} \right) \tag{4.42}$$

The base term for $\int (\nabla\phi)_T^2 \, d\,A$ is

$$\int ((\nabla\phi)^2 d\,A)_B = A_1^2 \int \cos^2 \omega t \, \sin^2 kx \, \cosh^2 k(z + H)_{z=-H} \, dx \, dy$$

$$= \frac{A_1^2}{4} L^2 \qquad (4.4\ldots)$$

The end wall terms are

$$A_1^2 \int \sinh^2 k(z + H) \, dy \, dz$$

$$= L \, A_1^2 \int \left[\frac{\cosh 2k(z + H) - 1}{2}\right] dz \qquad (4.44)$$

The side wall terms are

$$A_1^2 \left[\int \cos^2 kx \, \sinh^2 k(z + H) \, dx \, dz\right.$$

$$\left. + \int \sin^2 kx \, \cosh^2 k(z + H) \, dx \, dz\right]$$

$$= \frac{L \, A_1^2}{2} \int_{-H}^{0} \cosh 2k(z + H) \, dz \qquad (4.45)$$

Combining the contributions to $\int (\nabla\phi)_T^2 \, dA$ from the side walls and end walls yields

$$\frac{L A^2}{2} \int_{-H}^{0} \left(2 \cosh 2k(z + H) - 1\right) dz$$

$$= \frac{L A^2}{2} \frac{\sinh 2kH}{k} - H \qquad (4.46)$$

For a laterally mobile air-water surface S_F is given by

$$S_F = 2 \nu k^2 \qquad (4.47)$$

and for a laterally immobile surface

$$S_F = \sigma_B \cosh^2(kH) \qquad (4.48)$$

where σ_B = damping frequency due to the base [Pike and Curzon, 1968]. The results calculated above are of course for smooth surfaces. It has been shown that the enhancement in the damping due to a groove structure with an isosceles triangular or approximately sinusoidal cross section is directly proportional to the area ratio d A/d A_0. Thus for a grooved base, the base term (4.43) becomes

$$A' \frac{A_1^2}{4} L^2 \qquad (4.49)$$

Where A' = area ratio.

Using (4.42), (4.44)-(4.47) and (4.49), σ for a laterally mobile air-water interface is given by

$$\sigma = \left(\frac{\omega\nu}{2}\right)^{\frac{1}{2}} \frac{k}{\sinh kH} \left[A' + \frac{2H}{L}\left(\frac{\sinh 2kH}{kH} - 1\right)\right] + 2\nu k^2 \qquad (4.50)$$

For a laterally immobile surface

$$\sigma = \left(\frac{\omega\nu}{2}\right)^{\frac{1}{2}} \frac{k}{\sinh kH} \left[A' + \cosh^2(kH) + \frac{2H}{L}\left(\frac{\sinh 2kH}{kH} - 1\right)\right] \qquad (4.51)$$

If the surface is only partly covered, the factor $\cosh^2 kH$ is correspondingly decreased, i.e. a term $\varepsilon \cosh^2 kH$ and $(1 - \varepsilon)2\nu k^2$ will be incorporated, where $0 < \varepsilon < 1$).

Chapter 5

DAMPING EXPERIMENTS FOR LARGE AMPLITUDE GROOVES

5.1 Experimental System

In this experimental investigation, the case of large groove dimensions is considered $a >> \ell$. The same approach to the study of wave damping as given in Section 3.1 has been used (i.e. temporal damping is used throughout).

As has been remarked previously, contaminants (mono-layers) present on the free surface can significantly alter the damping of surface waves, causing problems in the experimental investigation of the effect of wall roughness on the damping. When two different surface modes are considered, however, it is possible to separate the contributions to the damping from the free surface and the base (see Section 5.2). In all of our experimental work (for $a >> \ell$), two surface modes have been used, where one satisfies the shallow fluid case ($kH << 1$) and the other satisfies the deep fluid case $kH \geq 1$.

The geometry of the square lucite wave tank used in this experimental investigation is shown in Figure 21.

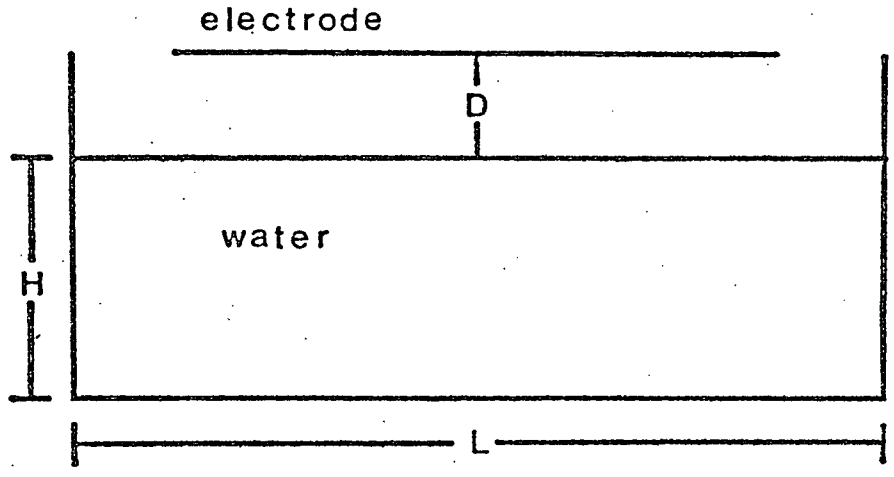

Figure 21. Cross-section of the square wave tank.

Essentially, the same experimental procedure, described in Section 3.1 has been used. A grooved aluminum plate could be mounted on the bottom of the tank and was secured on it with a silicone adhesive (General Electric RTV). This procedure was necessary in order to prevent anomalously large wave damping caused by seepage of the water under the grooved plate. The grooves on the plate were identical and parallel to one another, having a cross section in the form of an isosceles triangle (the groove dimensions are given in Table 2).

The waves are again excited by a horizontal electrode mounted above the fluid surface; the same electrode described previously is used. The electrode is suspended from a lucite cross fixed across the top of the tank. The height of the electrode above the fluid surface is adjusted by four levelling screws at the ends of the cross. In this series of experiments the electrode and water surface were separated by a constant distance of (1.9 ± 0.1) cm.

The high voltage wave generator used for this experiment was completely different from that used previously. The generator incorporates two novel features. All of generator timing is determined by a crystal controlled master clock. The output waveform of the generator is constructed by sequential scanning (with pulses from the master clock), of a series of voltage registers.

Table 2

Experimental Conditions

Features of the Water Tank	
Depth	= (3.01 ± 0.01) cm
Length, L	= (26.7 ± 0.1) cm
Kinematic viscosity	= 0.01 cm^2 sec^{-1}
Properties of Grooved Base	
Groove Spacing	= (3.2 ± 0.1) mm
Apex Angle	= 90°
A' (Area Ratio)	= $\sqrt{2}$
Characteristics of Modes	
Mode 1 (Sloshing Mode)	
Wave number, k	= 0.1178 cm^{-1}
Oscillation Frequency, f	= (1.020 ± 0.001) Hz
Boundary Layer Thickness = $\sqrt{\nu/2\pi f}$	= 0.40 mm
Mode 2	
Wave number, k	= 0.3533 cm^{-1}
Oscillation Frequency, f	= (2.630 ± 0.001) Hz
Boundary Layer Thickness	= 0.25 mm

A schematic diagram of the high voltage waveform generation circuit is shown in Figure 22. The pulses from the oscillator (crystal controlled) are divided by 10 and 800 in stages B and C respectively. The output from C is delayed by D (variable delay 0.5 - 2.5 msec). The output pulse from D occurs in coincidence with one of the pulses from B, and also resets B and C. Since the jitter in the delay unit output pulse is less than the interval between pulses coming from B, the timing accuracy is controlled by the jitter of the pulses coming from B. This jitter is less than 0.5 μsec.

This unit (B, C, and D) plus the oscillator produces high stability variable frequency output pulses. The output pulses from E (programmable divider National Semi-Conductor DM 7520) constitute the clock pulses which determine the rate at which the voltage registers contained in the function generator, are scanned. A schematic diagram of the function generator is shown in Figure 23. The memory consists of 16 storage registers. Each register has 128 levels, with level 128 corresponding to 5 volts and level zero to 0 volts. Thus each register can be programmed to any DC level from 0 to 5 volts. To construct any periodic positive waveform, one-half of the waveform is considered. This half waveform is then divided into 16 equal sections. The desired value of the waveform is then deposited by the use of the manual address in a successive storage register. To illustrate this

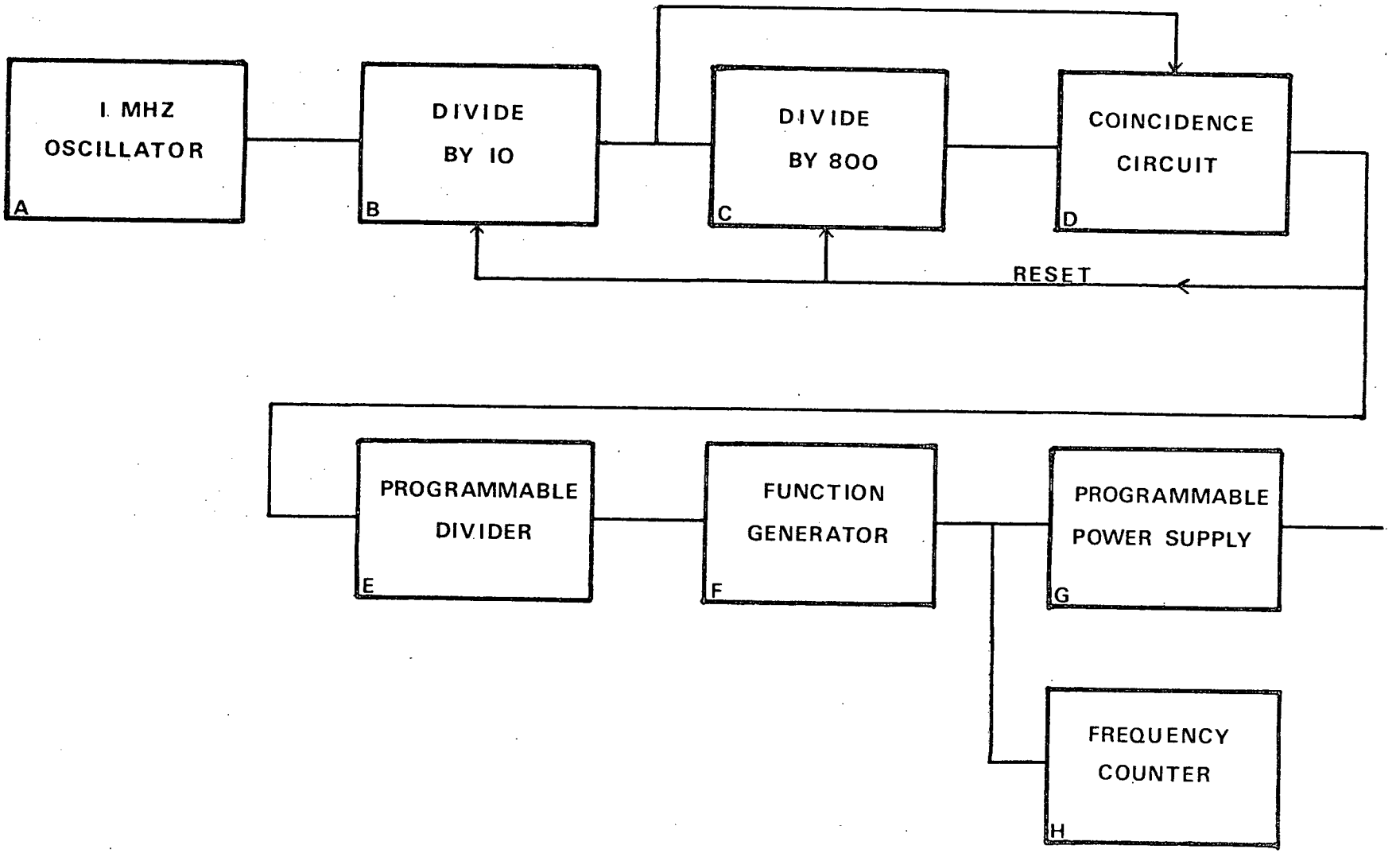

Figure 22. High voltage waveform generation circuit.

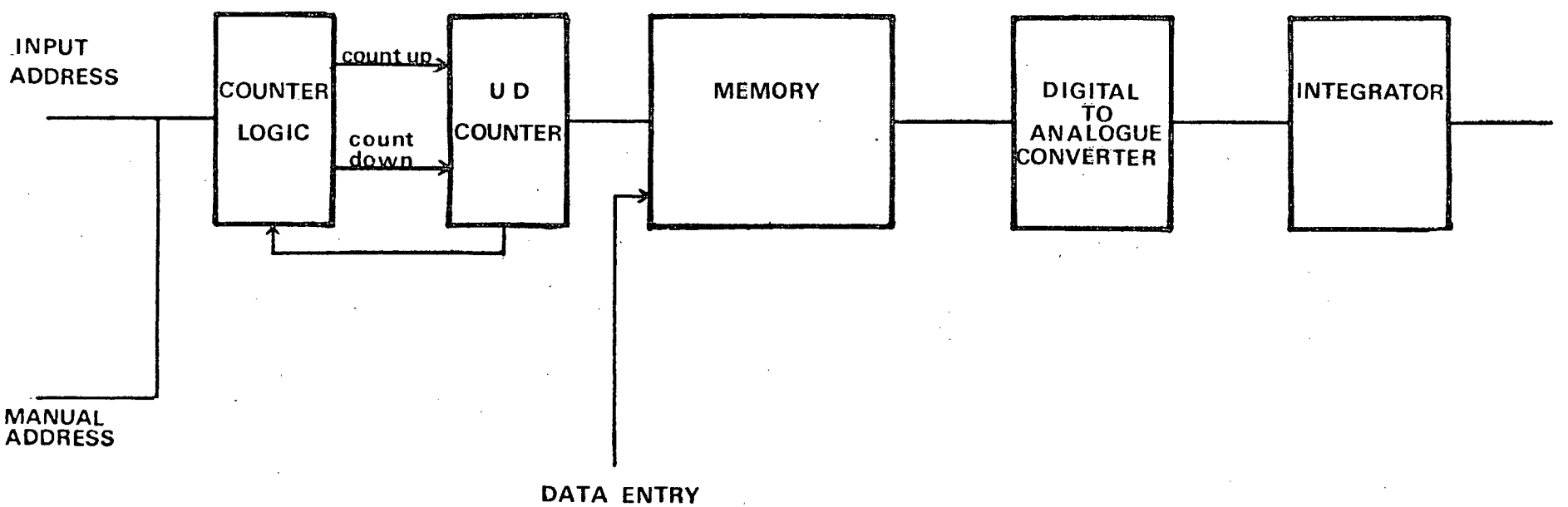

Figure 23. Function generator.

procedure, the programmed voltage levels of the registers to produce a simple output pulse (see Figure 24c) are shown in Figure 24a.

The output of the function generator is derived from the storage registers. When a clock pulse of frequency ω (this frequency being controlled by the output pulses from E) is applied to the input address, an output signal of $\omega/32$ is produced by sweeping up and down through the 16 successive registers of the memory. The counter logic and the UP/DOWN Counter control this sweeping through the registers. The scanning cycle for this is shown schematically in Figure 24b. The output from the memory (storage registers) is a digital signal and this is converted to an analogue result in the D/A converter. The buffer and integrator are used to smooth out the resulting waveform. For the register levels given in Figure 24a, the resultant output of the function generator would be as in Figure 24c, with the frequency of this output pulse being controlled by the pulses from E.

The output of the function generator is applied to a KEPCO programmable high voltage power supply. This unit operating in the programmable mode acts as a low frequency amplifier with a gain of 1000. The output of the Kepco unit is applied directly to the electrode.

Figure 24. The construction of an arbitrary waveform using the function generator.

(a) Register voltage (deposited by manual address system) vs register number

(b) Scanning cycle (determined by clock pulses from E (Figure 22) and switching logic of up-down counter

(c) Resultant waveform

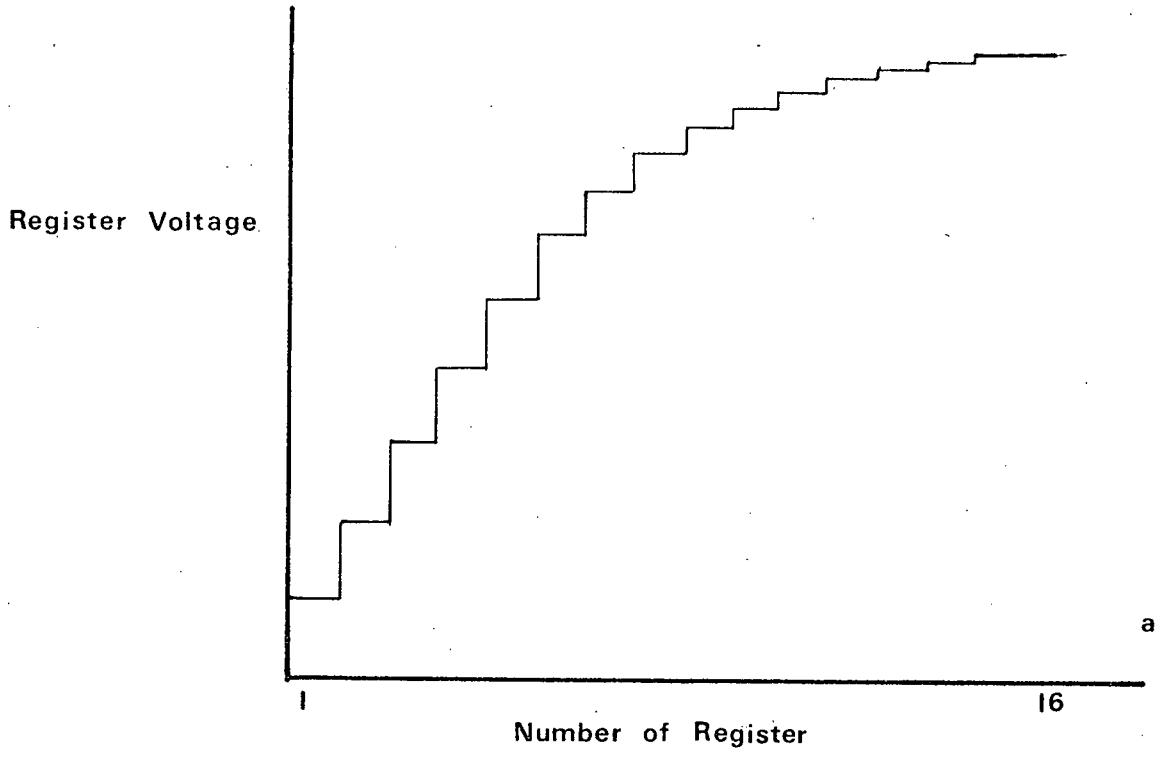
Register Voltage
a
1
16
Number of Register

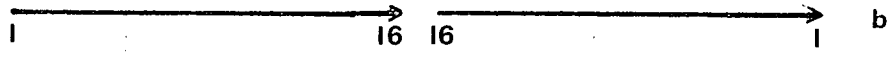
1
16
16
1
b

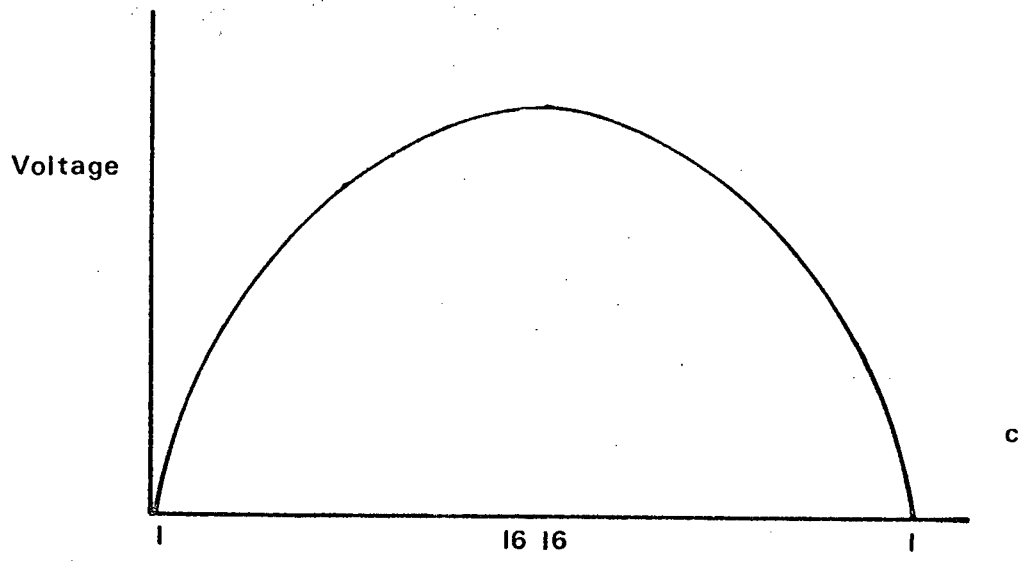
Voltage
c
1
16 16
1

5.2 Experimental Results and Discussion

Experiments were conducted to determine the damping frequency for both a smooth lucite base and a grooved base present in the wave tank. The experiments performed in this investigation were performed in an identical manner to those described in Section 3.1. As was remarked previously, two surface modes were considered in this investigation. By applying the high voltage waveform to one-half of the electrode surface modes of wavelength (λ), 2L and (2/3)L can be excited, where L is the length of the wave tank. The frequency of the high voltage waveform is adjusted to resonate with the mode considered (1.02 Hz for 2L and 2.63 for (2/3)L).

Initially the damping frequency for the smooth base was determined for two flow directions (separated by 90°). This was done to ensure that the wave tank did not possess any directional damping properties. If this had not been checked, any directional damping effects with the grooved base present might erroneously have been attributed to the grooves.

For the smooth base we found no directional damping properties. With the grooved base present, damping runs were conducted for flow parallel as well as transverse to the grooves, for both modes. In our initial runs, we thought we had discovered a directional damping effect with the grooved base present. The damping for flow parallel to the grooves

was consistently larger than for flow transverse to the grooves. This result was reproducible; the value of the damping frequency was not. On close examination of the silicone adhesive, which secures the grooved base to the bottom of the tank, we found small cracks in the sealer which allowed water to get under the base. These cracks were located mid-way along one wall, where the plane of this wall was transverse to the grooves. This accounted for the directional damping effects. For flow along the grooves the velocity at the cracks in the sealer would be large, and there would be enhancement of the damping due to flow into these cracks. For flow transverse to the grooves, the cracks are essentially on the nodal line where the flow velocity is a minimum. The enhancement in the damping caused by the cracks in the silicone sealer would thus be smaller for this case (flow transverse to grooves) than for flow parallel to the grooves. After these cracks were properly sealed, *no* directional damping effect was observed. Typical damping runs are shown in Figure 27-28. The straight lines are determined by a least squares fit to the data points. The oscilloscope traces from which these graphs are derived (Figure 27-28) are shown in Figure 25-26. It will be noted that the amplitudes for Figures 25a, 25b and 26a, 26b are different. This is due to the position of the detector and the time after switch-off of the field at which the recording

Figure 25. Damping runs for $\lambda = \frac{2}{3} L$ (horizontal scale 0.05 v/div, vertical scale 2 sec/div).

(a) smooth base

(b) smooth base with flow direction rotated 90° with respect to (a)

(c) grooved base with flow parallel to the grooves

(d) grooved base with flow transverse to the grooves

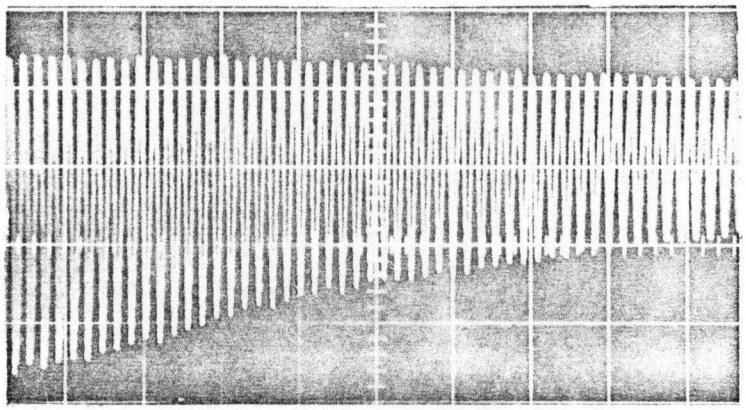

a

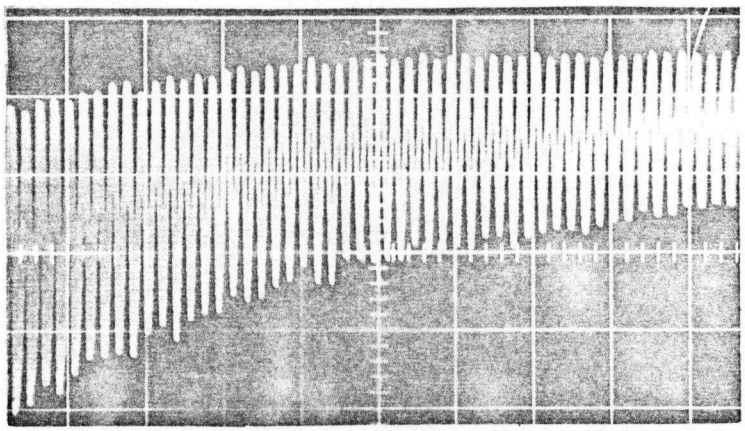

b

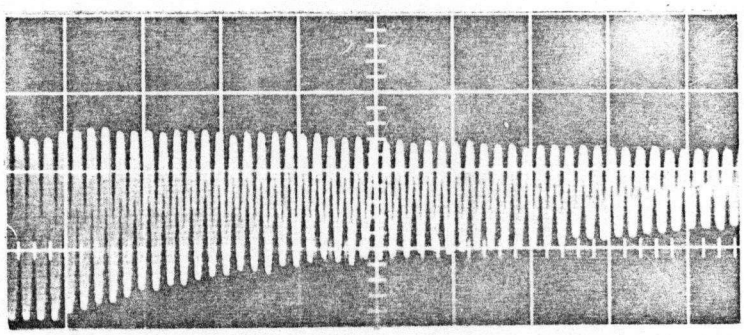

c

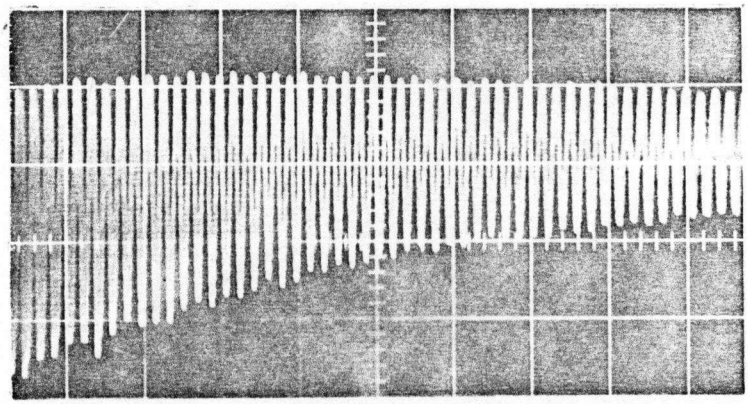

d

Figure 26. Damping runs for $\lambda = 2L$ (horizontal scale 5 sec/div).

(a) smooth base (vert. 0.05 v/div)

(b) smooth base with flow direction rotated 90° with respect to (a) (vert. 0.1 v/div and 0.05 v/div)

(c) grooved base with flow parallel to the grooves (vert. 0.1 v/div and 0.05 v/div)

(d) grooved base with flow transverse to the grooves (vert. 0.2, 0.1 and 0.05 v/div)

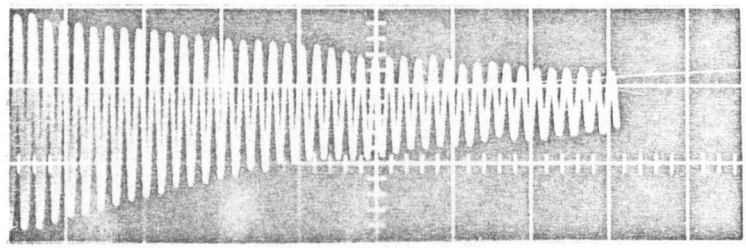

a

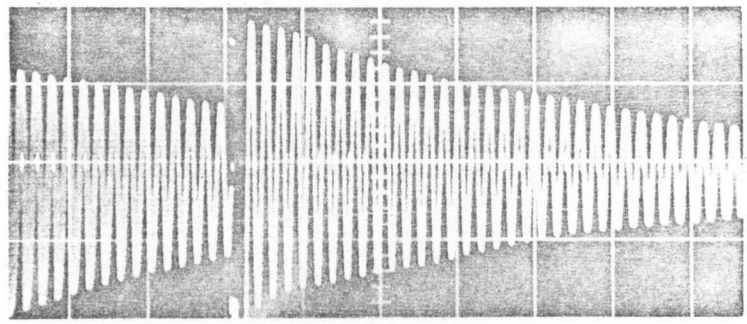

b

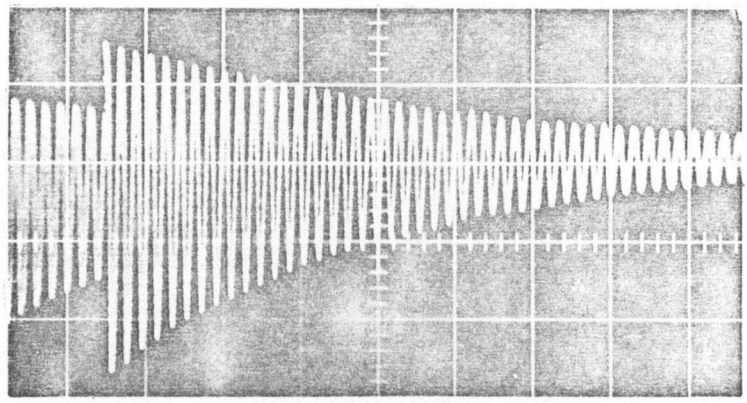

c

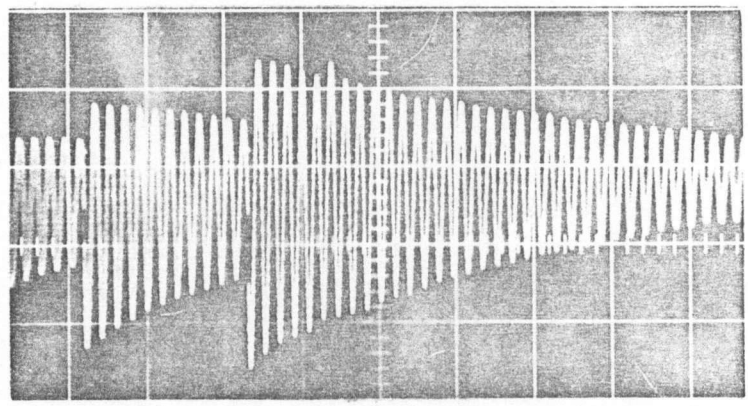

d

Figure 27. The logarithm of wave amplitude vs time ($\lambda = \frac{2}{3} L$).

(a) smooth base

(b) smooth base with flow direction rotated 90° with respect to (a)

(c) grooved base with flow parallel to grooves

(d) grooved base with flow transverse to grooves

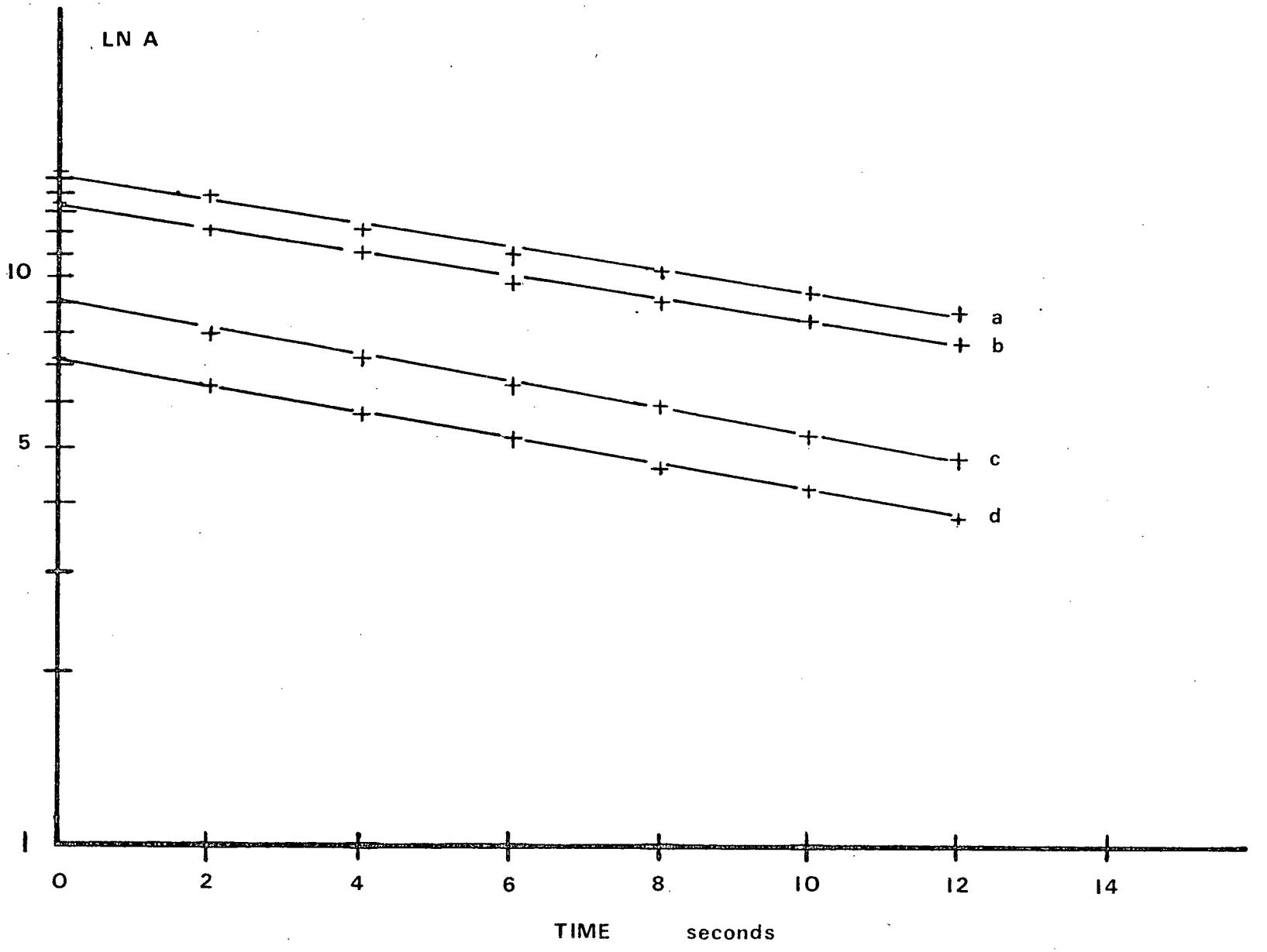
LN A
10
5
1
a
b
c
d
0
2
4
6
8
10
12
14
TIME seconds

Figure 28. The logarithm of wave amplitude vs time ($\lambda = 2L$).

(a) smooth base

(b) smooth base with flow direction rotated by 90° with respect to (a)

(c) grooved base with flow parallel to grooves

(d) grooved base with flow transverse to grooves

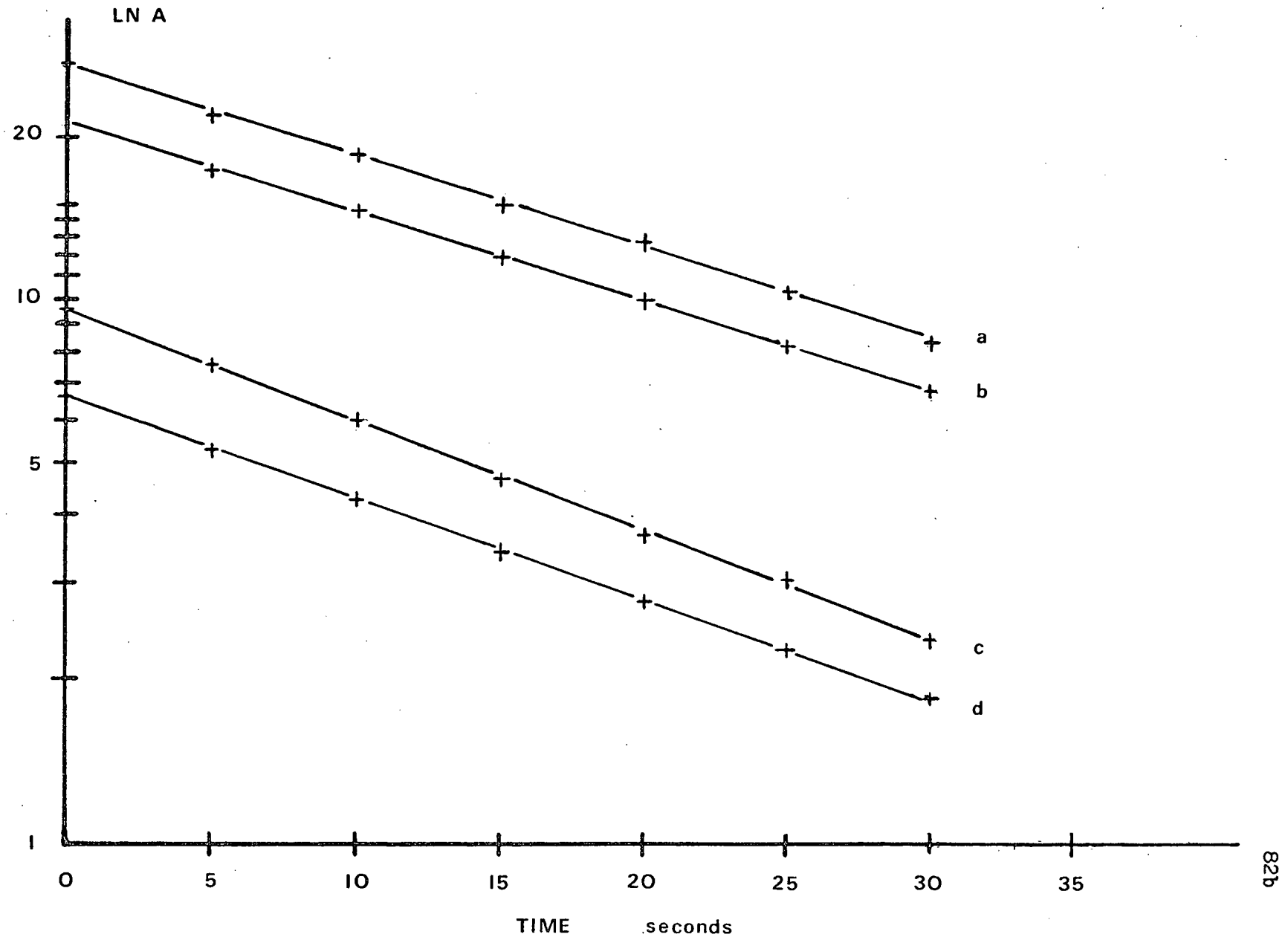
LN A
20
10
5
1
a
b
c
d
0
5
10
15
20
25
30
35
TIME seconds

of the amplitude started. From these graphs, it can be seen that the damping frequency is independent of the direction of the flow velocity with respect to the grooves, for both modes considered.

In our earlier experiments reproducibility had been a problem. In these runs distilled water from a copper distillation system had been used. In our later runs low conductivity distilled water from a glass system was used. Before a series of runs, the wave tank was rinsed out with this distilled water before filling the tank. With these precautions, reproducible results were obtained for the damping frequency.

According to the theoretical model developed in Section 4.2, the damping over grooved surfaces should be independent of the flow direction, and the enhancement in the damping should be proportional to the fractional area increase of the surface. When comparing our experimental results with this theory, it is essential to consider how well the experimental conditions approximate the theoretical model.

The grooved aluminum base used in these experiments satisfies all of the assumptions used in the theoretical model. The shortest wavelength surface mode has a length of ~ 18 cm, which is much larger than the groove spacing (~ 0.3 cm). The groove depth is also much smaller than the fluid depth (~ 3 cm). Finally the thickest boundary layer

used (for the lowest frequency mode) is $\lesssim$ 10% of the groove spacing (see Table 3).

Another effect which could cause a discrepency between the experimental conditions and that of the theory, is the condition of the air-water interface. In Section 4.3 the damping frequency is calculated for a laterally mobile and laterally immobile surface. The condition of the air-water interface may, however, be neither of the above; a surfactant monolayer might cover only a part of this surface.

In Table III the predictions of equation (4.50) for the damping frequency for a laterally mobile surface and equation (4.51) for a laterally immobile surface are given for both modes. The experimental σ from Figure 27-28 are also tabulated. The uncertainty in σ is ~ 1%. As Table 3 shows, for both modes the experimental results are well described by the predictions of equation (4.50) (the laterally mobile surface layer thoery).

From Table 3, it can be seen that the theoretical values for a laterally immobile surface are too large to account for the observed values of σ. If a monolayer were present on only a part of the surface σ would be larger than the laterally mobile values. There would not be good agreement between theory and experiment for this case. Hence, we are dealing with a laterally mobile surface layer in these experiments. The good agreement between our experimental results and the results.

Table 3

Values of the Damping Frequency, σ (sec^{-1})

Mode 1 (wavelength = 2 L)	Experimental (± 1%)	Theory (Laterally mobile air-water interface)	Theory (Laterally immobile air-water interface)
smooth base	0.035	0.034	0.064
grooved base	0.045	0.045	0.075
Mode 2 (wavelength = 2L/3)			
smooth base	0.039	0.041	0.105
grooved base	0.050	0.052	0.115

predicted by equation (4.50) confirm that the enhancement in the damping caused by a grooved base is proportional to the fractional area increase of the base.

5.3 Conclusions

There are two significant (and surprising) results which have been established in Part B. It was shown both theoretically and experimentally (for a square wave tank with a grooved base satisfying $a >> \ell$), that the damping is independent of the flow direction with respect to the grooves; and the damping is increased at a rate proportional to the area increase of the base (for triangular and approximately sinusoidal groove cross sections). The former result is the more surprising, since intuitively it would seem that the damping for a grooved base should be dependent on flow direction. This simple intuitive prediction has been shown in Part B not to be valid.

It has been established in Part A for $a < \ell$ that the variability in the damping is due to surfactants. Observations of damping then (particularly in space, rather than in time) should provide a very convenient method of studying the dynamic properties of two-dimensional physical systems. Non-uniform surface films could be studied by applying a high frequency electric field to the water surface. Regions of high damping (large concentration of surfactants) would then be low amplitude regions.

REFERENCES

1. M. Abramowitz and I.A. Stegun (1965). Handbook of mathematical functions (Dover Publications, Inc., New York.

2. K.M. Case and W.C. Parkinson, J. Fluid Mech., 2, 172 (1957).

3. F.L. Curzon and R.L. Pike, Can. J. Phys., 46, 2001 (1968).

4. F.L. Curzon and M.G.R. Phillips, Can. J. Phys., 51, 2175 (1973).

5. R. Dorrestein, Proc. Koninkl. Ned. Akad. Wetenschap, BB4, 260 and 350 (1951).

6. G.N. Ionides and F.L. Curzon, Can. J. Phys., 49, 2733 (1971).

7. G.N. Ionides and F.L. Curzon, Can. J. Phys., 50, 2698 (1972).

8. G.N. Ionides (1972). Ph.D. dissertation (University of British Columbia).

9. L.D. Landau and E.M. Lifshits (1959). Fluid Mechanics (Pergamon Press, Lond, New York).

10. V.G. Levich, Acta. Physicochim., U.S.S.R., 14, 307 and 321 (1941).

11. V.G. Levich, Physiochemical Hydrodynaimcs, Chapter 11 (Prentice Hall, N.J., 1968).

12. N. Levinson and R.M. Redheffer (1970). Complex Variables (Holden-Day Inc., San Francisco, London).

13. R.L. Pike and F.L. Curzon, Can. J. Phys., 46, 2009 (1968).

14. R.L. Pike (1967). Ph.D. dissertation (University of British Columbia.

15. M.R. Spiegel. Complex Variables (Schaum Publishing Co., N.Y.).

APPENDIX A

THE GENERAL RESULT FOR THE DAMPING FREQUENCY

$$\text{Derivation of } \sigma = \frac{1}{2}\left(\frac{\omega\nu}{2}\right)^{\frac{1}{2}}\left[\frac{\int(\nabla\phi)_T^2\, dA}{\int(\nabla\phi)^2\, d\tau}\right]$$

Consider a wave tank geometry as given by Figure 20. The damping frequency due to the walls of the wave tank will now be calculated. Without loss of generality, σ due to one surface will be determined and the form of this result will be applied to the other surfaces. In particular, this will be done for the bottom surface of the wave tank.

The equation of motion for a viscous fluid, given previously is

$$\rho\frac{\partial \underline{v}}{\partial t} = -\nabla P - \rho g + \nu\rho\nabla^2\,\underline{v} \qquad (A.1)$$

where

$$\underline{v} = \underline{v_0} + \underline{v_1};\ \underline{v_0} = \nabla\phi \qquad (A.2)$$

Equation (A.1) is now multiplied by $\underline{v}$ and the equation is integrated over the fluid volume.

$$\int \left[\frac{\partial}{\partial t} \left(\rho \frac{v^2}{2} \right) + \underline{v} \cdot (\nabla P + \rho g) \right] d\tau = \int \rho \left[\nu \, \underline{v} \cdot \nabla^2 \, v \right] d\tau \qquad (A.3)$$

In the absence of viscosity the RHS of (A.3) is zero. The term $\underline{v} \cdot (\nabla P + \rho g)$ must then be the rate of change of the potential energy, i.e. $\underline{v} \cdot (\nabla P + \rho g) = \frac{\partial}{\partial t}$ (P.E.). The LHS of (A.3) is then the time rate of change of the total energy E_T

$$\frac{\partial}{\partial t} \int E_T \, d\tau = \int \rho \nu \, \underline{v} \cdot \nabla^2 \, \underline{v} \, d\tau \qquad (A.4)$$

Since σ caused by the bottom surface is to be calculated v_1 will have the form

$$v_1 \sim \left(\nabla \phi(t) \right)^{\dagger} \exp \left[- z(1 + i)\gamma + i \, \omega \, t \right] \qquad (A.5)$$

where $\gamma = \frac{1}{\sqrt{2} \, \ell}$

Now in equation (A.4) the quantities we are interested in are the real parts of the velocity terms, i.e.

$$\int (\mathrm{Re} \, \underline{v}) \cdot (\mathrm{Re} \, \nabla^2 \, v_1) \, d\tau$$

$$= \int (\mathrm{Re} \, v_0)(\mathrm{Re} \, \nabla^2 \, v_1) \, d\tau + \int (\mathrm{Re} \, v_1)(\mathrm{Re} \, \nabla^2 \, v_1) \, d\tau \qquad (A.6)$$

---

†Note that $\nabla\phi$ is evaluated on the boundary, i.e. bottom surface of the tank.

Now for v_1 in the form given by (A.5)

$$\overline{(\mathrm{Re}\ v_1)(\mathrm{Re}\ \nabla^2\ v_1)} = \mathrm{Re}(v_1\ (\nabla^2\ v_1)^*) \tag{A.7}$$

where the bar above the expressions on the LHS indicates a time average over many oscillations of the surface. The second term of (A.6) is then

$$\int \overline{(\mathrm{Re}\ v_1)(\mathrm{Re}\ \nabla^2\ v_1)}\ d\tau = \mathrm{Re} \int v_1(1 + i)^2\ \gamma^2\ v_1^*\ d\tau$$

$$= \mathrm{Re}\left[\int |v_1|^2\ 2i\ \gamma^2\ d\tau\right] = 0 \tag{A.8}$$

The first term of (A.6) is

$$\int \mathrm{Re}\left[v_0\ \nabla^2\ v_1^*\right]\ d\tau = \mathrm{Re} \int (v_0)\ \left[\frac{\partial v_1}{\partial z}\right]^*\ dA \tag{A.9}$$

where dA is a surface element on the bottom of the tank.

The boundary conditions on the surfaces of the tank are that $\underline{v} = 0$. Equation (A.9) then becomes

$$\mathrm{Re}\left[-\gamma \int (1 + i)\left[\nabla\phi(t)\right]^2 dA\right]$$

$$= -\gamma \int \left[\nabla\phi(t)\right]^2\ dA \tag{A.10}$$

The total energy is given by

$$\int \rho \left[\nabla\phi(t)\right]^2 \, d\tau$$

Equation (A.4) is then given by

$$\frac{\partial}{\partial t} \int \rho \left[\nabla\phi(t)\right]^2 \, d\tau = -\nu \, \gamma \rho \int \left[\nabla\phi(t)\right]^2 \, dA \qquad (A.11)$$

For convenience $\nabla\phi(t)$ can be broken into a spatial part and a time dependent part

$$\nabla\phi(t) = \left[\nabla\phi\right]_S \, f(t) \qquad (A.12)$$

where $\frac{\partial}{\partial t} \left[\nabla\phi\right]_S = 0.$

For a linear viscous fluid which is damping (i.e. driving mechanism has been turned off) the inviscid velocity will decay exponentially with time. Hence f(t) is given by

$$f(t) \sim e^{-\sigma t} \qquad (A.13)$$

where σ is the damping frequency. Equation (A.11) then becomes

$$\frac{\partial}{\partial t}\left[f(t)^2\right] \int \left(\nabla\phi\right)_S^2 = -\nu\ \gamma\ f(t)^2 \int \left(\nabla\phi\right)_S^2 dA$$

$$\frac{\partial f(t)}{\partial t} = \frac{-\nu\ \gamma\ f(t)}{2} \frac{\int (\nabla\phi)_S^2\ dA}{\int\ (\nabla\phi)_S^2\ d\tau} \tag{A.14}$$

$$\therefore\ \sigma = \frac{1}{2}\left(\frac{\omega\nu}{2}\right)^{\frac{1}{2}} \frac{\int\ (\nabla\phi)_S^2\ dA}{\int\ (\nabla\phi)_S^2\ d\tau} \tag{A.15}$$

The result (A.15) is completely general and can be applied to any surface of the tank, the surface integration being over the surface considered. The total σ is then the sum of σ from all of the surfaces of the wave tank.